Chem, Volume *8*

Supplemental information

Porous polyisothiocyanurates for selective palladium recovery and heterogeneous catalysis

Kyung Seob Song, Timur Ashirov, Siddulu Naidu Talapaneni, Adam Hugh Clark, Alexander V. Yakimov, Maarten Nachtegaal, Christophe Copéret, and Ali Coskun

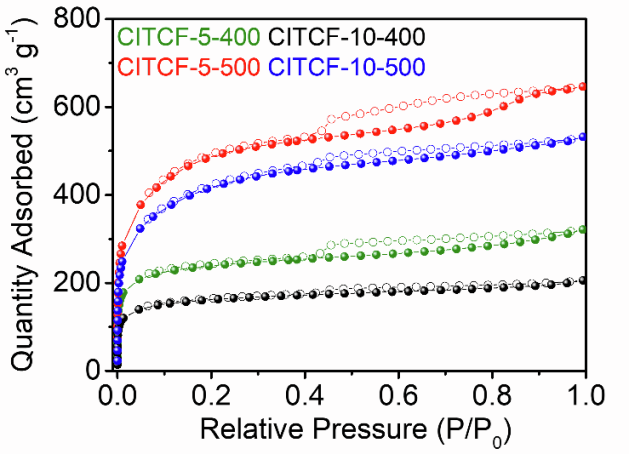

Figure S1. Optimization of reaction conditions for the synthesis of CITCFs (See also Figure 3). Ar adsorption (filled) and desorption (empty) isotherms of CITCFs obtained at 77 K of CITCFs. CITCF-X-Y represents X = mole ratio of $ZnCl_2$ with respect to the precursor (1:5 and 1: 10), Y = reaction temperature of 400 and 500 °C. CITCFs synthesized using 5 eq. of $ZnCl_2$ showed the highest surface area.

Table S1. BET surface area of CITCFs (See also Table1)

Sample	BET [a], ($m^2\ g^{-1}$)	Langmuir, ($m^2\ g^{-1}$)	S_{micro} [b] ($m^2\ g^{-1}$)	S_{ext} ($m^2\ g^{-1}$)	V_{total} [c] ($cm^3\ g^{-1}$)	V_{micro} [d] ($cm^3\ g^{-1}$)	d_{micro} [e] (nm)
CITCF-5-400	780	929	581	198	0.41	0.2	0.47
CITCF-5-500	1589	1901	772	817	0.89	0.25	0.47
CITCF-10-400	525	628	353	172	0.26	0.13	0.5
CITCF-10-500	1347	1635	665	682	0.72	0.23	0.47

[a] BET surface area calculated over the pressure range (P/P_0) obtained from Rouquerol plots. [b] Micropore surface area calculated from the adsorption isotherm using the *t*-plot method. [c] Total pore volume obtained at $P/P_0 = 0.99$. [d] Micropore volume calculated using the t-plot method. [e] Micropore diameter calculated from NLDFT method.

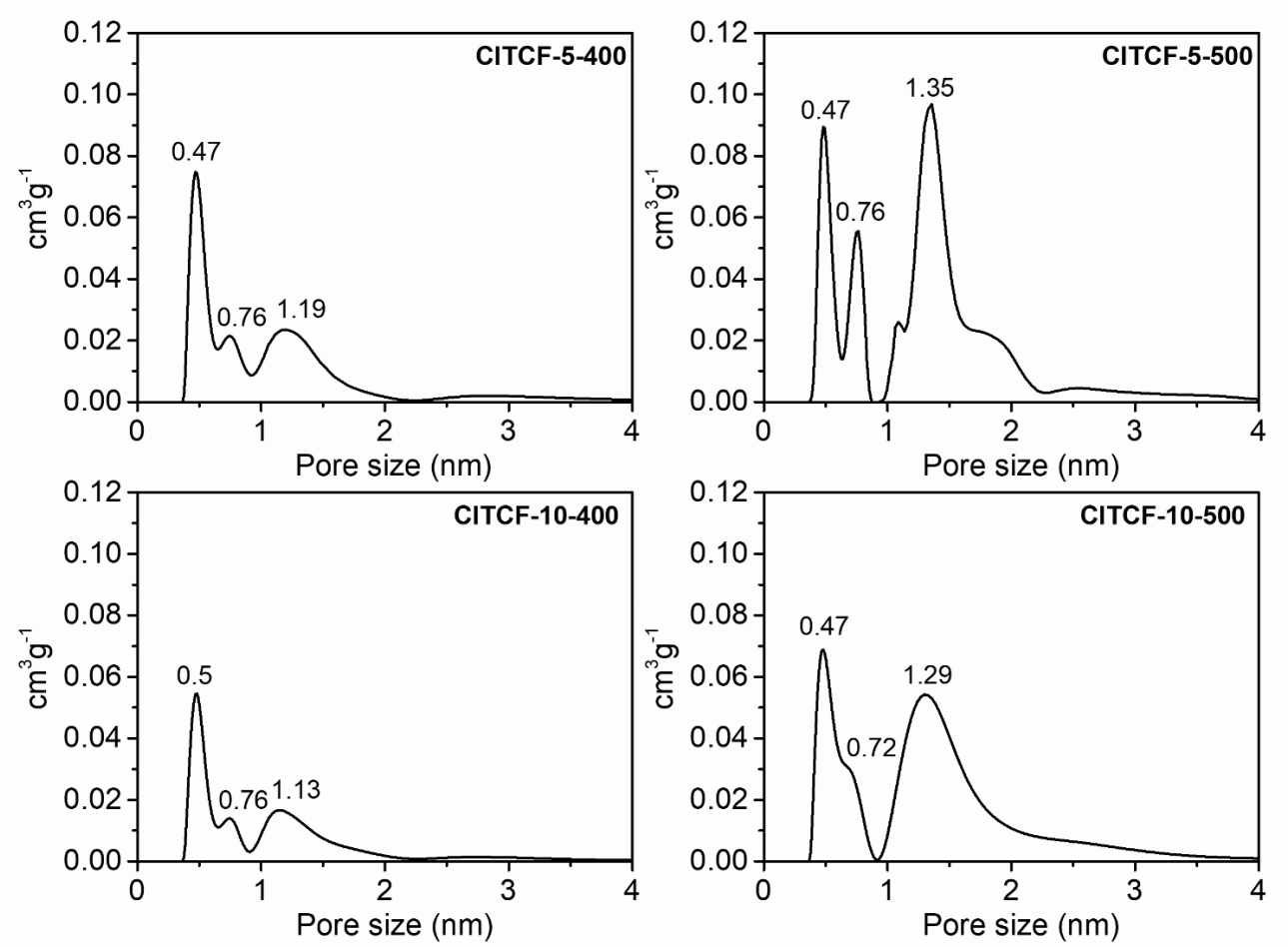

Figure S2. NLDFT pore size distribution (PSD) of CITCFs (See also Figure 3). CITCF-X-Y represents X = mole ratio of $ZnCl_2$ with respect to the precursor (1:5 and 1: 10), Y = reaction temperature of 400 and 500°C.

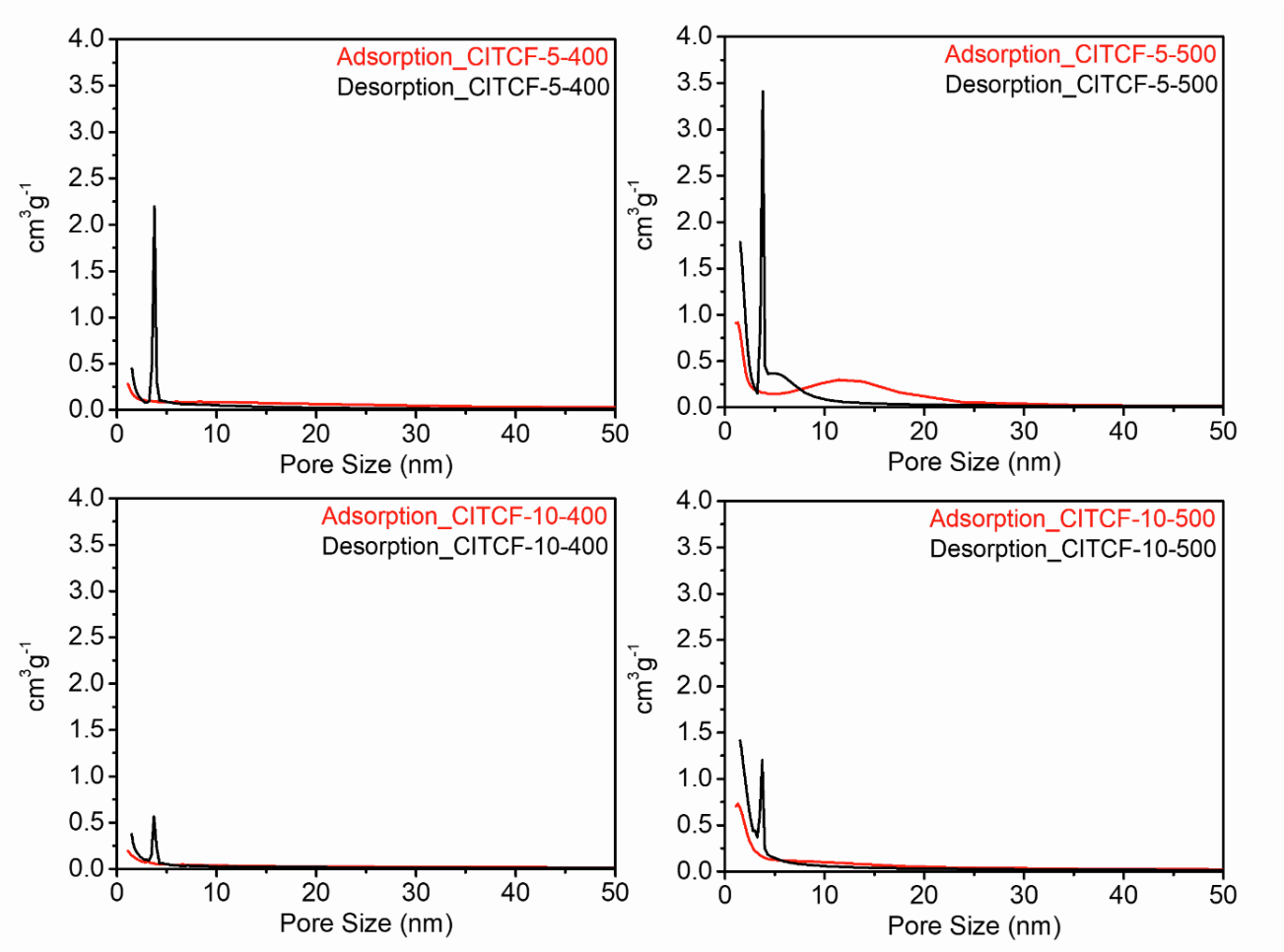

Figure S3. BJH pore size distribution analysis of CITCFs. CITCF-X-Y represents X = mole ratio of $ZnCl_2$ with respect to the precursor (1:5 and 1: 10), Y = reaction temperature of 400 and 500 °C.

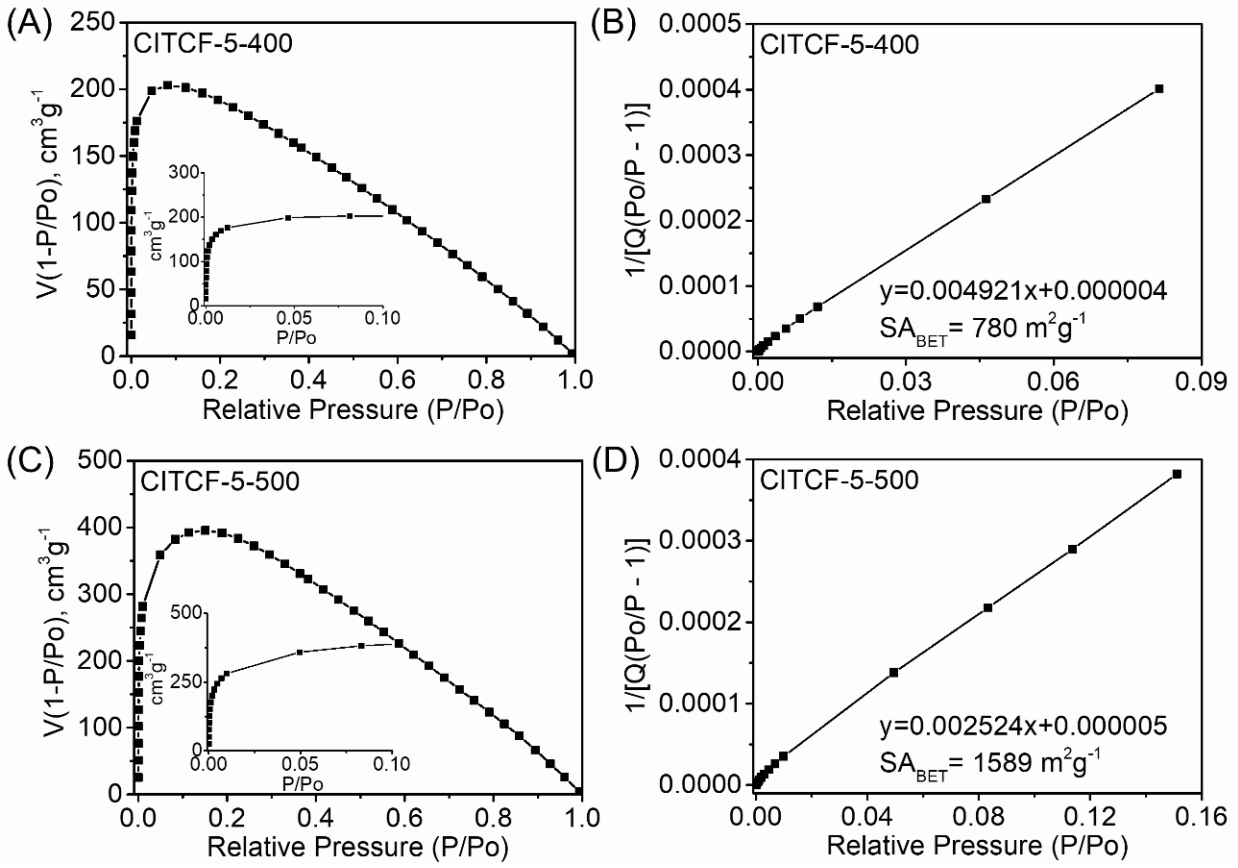

Figure S4. Rouquerol plots and BET linear plots of (A), (B) CITCF-5-400 and (C), (D) CITCF-5-500. CITCF-X-Y represents X = mole ratio of $ZnCl_2$ with respect to the precursor (1:5 and 1: 10), Y = reaction temperature of 400 and 500 °C.

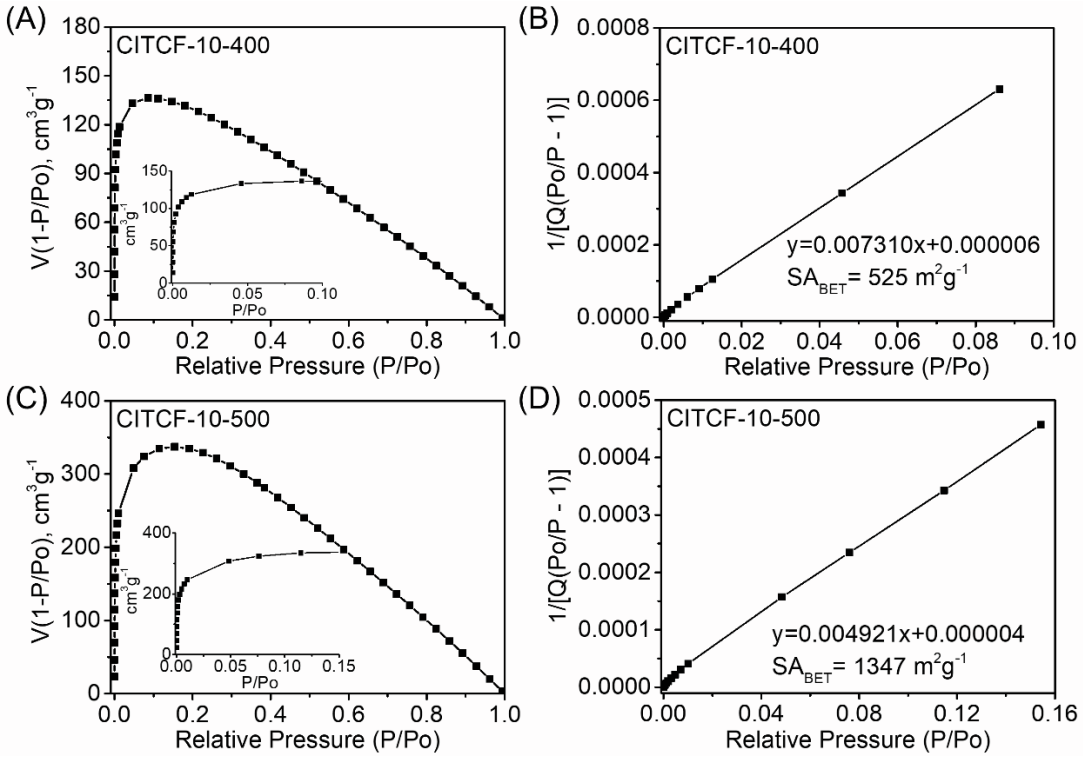

Figure S5. Rouquerol plots and BET linear plots of (A), (B) CITCF-10-400 and (C), (D) CITCF-10-500. CITCF-X-Y represents X = mole ratio of $ZnCl_2$ with respect to the precursor (1:5 and 1: 10), Y = reaction temperature of 400 and 500 °C.

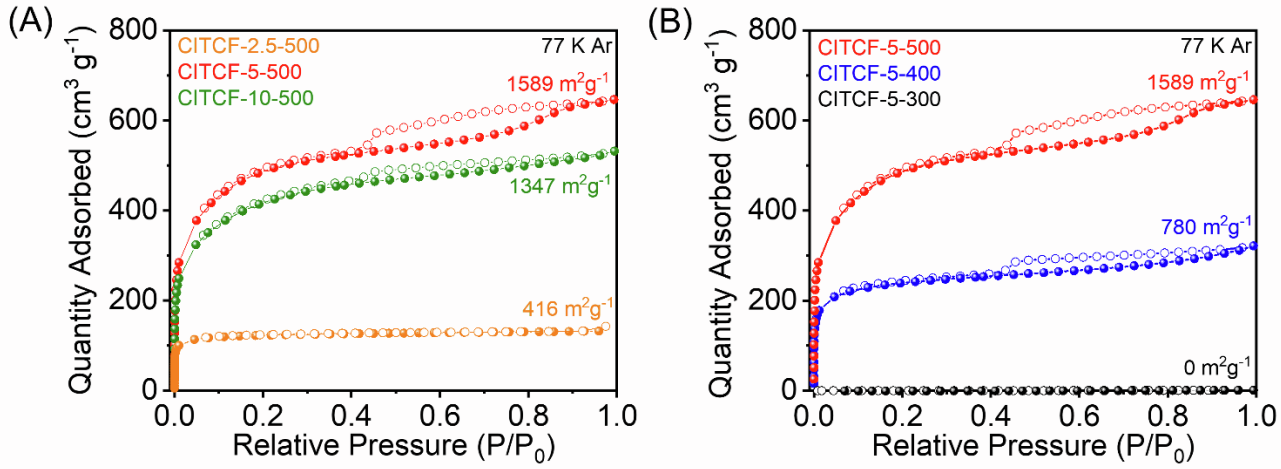

Figure S6. The impact of $ZnCl_2$ amount on the surface area of CITCFs. CITCF-X-Y represents X = mole ratio of $ZnCl_2$ with respect to the precursor (1:5 and 1: 10), Y = reaction temperature of 300, 400 and 500 °C. (A) The effect of $ZnCl_2$ mole ratio and (B) the reaction temperature on the porosity of CICTFs.

Table S2. The impact of $ZnCl_2$ amount on the surface area of CITCFs.

Sample	BET [a], ($m^2\ g^{-1}$)	Langmuir, ($m^2\ g^{-1}$)	S_{micro} [b] ($m^2\ g^{-1}$)	S_{ext} ($m^2\ g^{-1}$)	V_{total} [c] ($cm^3\ g^{-1}$)	V_{micro} [d] ($cm^3\ g^{-1}$)
CITCF-2.5-500	416	507	373	43	0.17	0.13
CITCF-5-500	1589	1901	772	817	0.89	0.25
CITCF-10-500	1347	1635	665	682	0.72	0.23

[a] BET surface area calculated over the pressure range (P/P_0) obtained from Rouquerol plots. [b] Micropore surface area calculated from the adsorption isotherm using the t-plot method. [c] Total pore volume obtained at P/P_0 = 0.99. [d] Micropore volume calculated using the *t*-plot method.

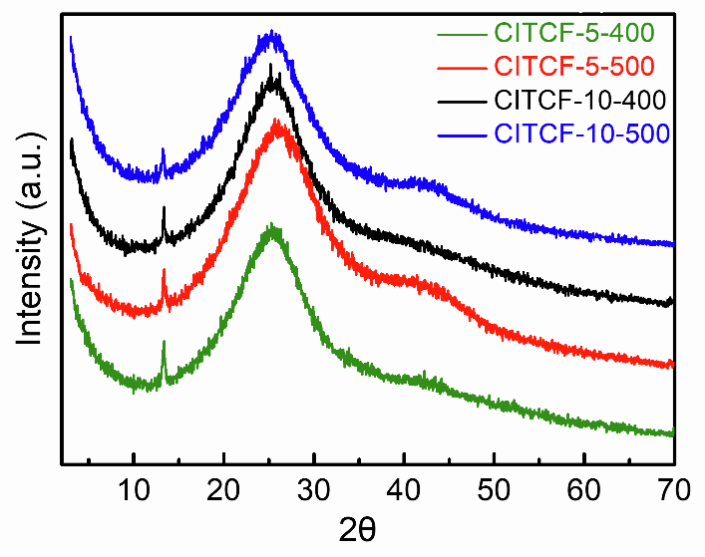

Figure S7. PXRD Analysis of CITCFs. CITCF-X-Y represents X = mole ratio of $ZnCl_2$ with respect to the precursor (1:5 and 1: 10), Y = reaction temperature of 400 and 500 °C.

Supplemental Experimental Procedures

Synthesis of Model Compounds:

Synthesis of 1,3,5-triphenyl-1,3,5-triazine-2,4,6-trithione (Model Compound 1): Phenyl isothiocyanate (0.8 mmol, 108 mg) and the salt mixture of NaCl/KCl/ZnCl (1.05 mmol, 2.65 mmol, 4.15 mmol, total 830 mg) are transferred into a Pyrex ampoule under an inert atmosphere. The ampoules were evacuated and sealed at room temperature. Then, the ampoule was transferred into a box furnace and the temperature was raised to 250 °C (3 °C min^{-1} ramping) and kept it under these conditions for 24h. Afterwards, the ampoule was cooled down to room temperature and opened carefully. The black colored crude product was crushed, transferred to ethyl acetate (200 mL) and stirred for 1 h. The solid was removed by filtration and the dark brownish filtrate was washed with H_2O. The organic phase was dried using Na_2SO_4 and concentrated under vacuum. The model compound 1 was isolated by preparative TLC using ethyl acetate/hexane (1:9) mixture as the mobile phase.

1,3,5-triphenyl-1,3,5-triazine-2,4,6-trithione ^{1}H-NMR (500 MHz, $CDCl_3$) δ = 7.52 (t, 6H), 7.45 (t, 3H), 7.32 (d, 6H) ppm. ^{13}C-NMR (500 MHz, $CDCl_3$) δ = 172.7 (C=S), 143.9 (NC_{Ar}), 129.9 ($2CH_{Ar}$), 129.1 (CH_{Ar}), 128.5 ($2CH_{Ar}$) ppm. HRMS: m/z = 406.0506 $[M + H]^+$ (calc. for $C_{21}H_{16}N_3S_3$: 406.0506). Yield 5 %.

Synthesis of 1,3,5-tri([1,1'-biphenyl]-4-yl)-1,3,5-triazine-2,4,6-trithione (Model Compound 2): 4-biphenyl isothiocyanate (0.8 mmol, 211 mg) and the salt mixture of NaCl/KCl/ZnCl (1.05 mmol, 2.65 mmol, 4.15 mmol, total 830 mg) are transferred into a Pyrex ampoule under an inert atmosphere. The ampoules were evacuated and sealed at room temperature. Then, the ampoule was transferred into a box furnace and the temperature was raised to 250 °C (3 °C min^{-1} ramping) and kept under these conditions for 24 h. Afterwards, the ampoule was cooled down to room temperature and opened carefully. The dark brownish crude was crushed, transferred to dichloromethane (200 mL) and stirred for 1 h. The dark orange solution filtered to remove the remaining solids and the filtrate was washed with H_2O. The organic phase was dried using Na_2SO_4 and concentrated under vacuum. The model compound 2 was isolated by preparative TLC using dichloromethane/hexane (1:2) as the mobile phase.

1,3,5-tri([1,1'-biphenyl]-4-yl)-1,3,5-triazine-2,4,6-trithione ^{1}H-NMR (500 MHz, $CDCl_3$) δ = 7.73 (d, 6H), 7.66 (d, 6H), 7.44 (t, 6H), 7.41 (d, 6H), 7.36 (t, 3H) ppm. ^{13}C-NMR (500 MHz, $CDCl_3$) δ = 172.7 (C=S), 142.9 (NC_{Ar}), 141.9 (CC_{Ar}), 139.9 (CC_{Ar}), 128.9 ($2CH_{Ar}$), 128.8 ($2CH_{Ar}$), 128.6 ($2CH_{Ar}$), 127.9 (CH_{Ar}), 127.4 ($2CH_{Ar}$) ppm. MALDI: m/z = 740.3802 $[M + Ag^+]$ (calc. for $C_{39}H_{27}AgN_3S_3^+$: 740.0413). Yield 54 %.

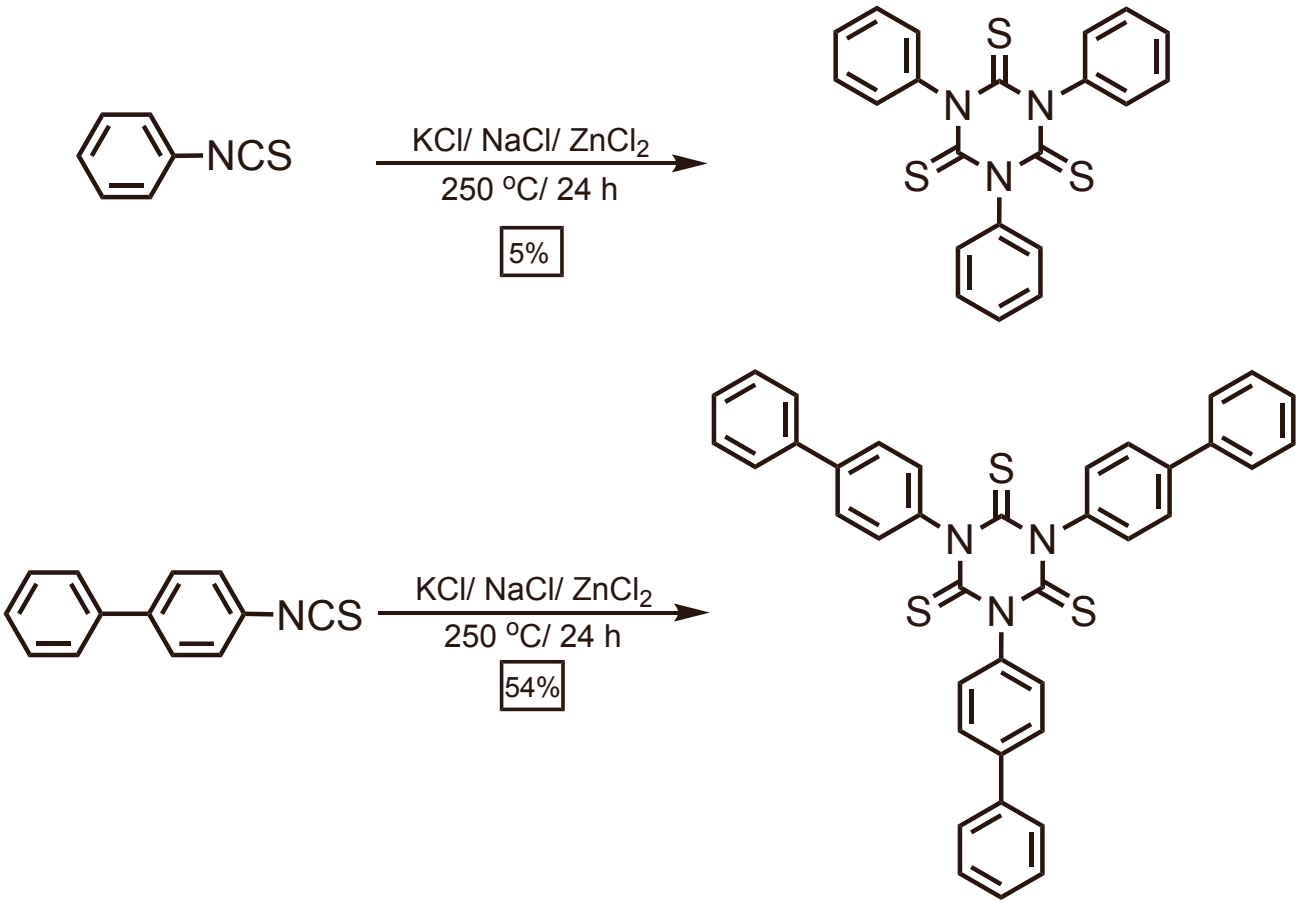

Scheme S1. Synthetic scheme for the preparation of model compounds under ionothermal conditions. 1,3,5-triphenyl-1,3,5-triazine-2,4,6-trithione **(Model Compound 1)** and 1,3,5-tri([1,1'-biphenyl]-4-yl)-1,3,5-triazine-2,4,6-trithione **(Model Compound 2)** were obtained from phenylisothiocyanate and 4-biphenyl isothiocyanate, respectively.

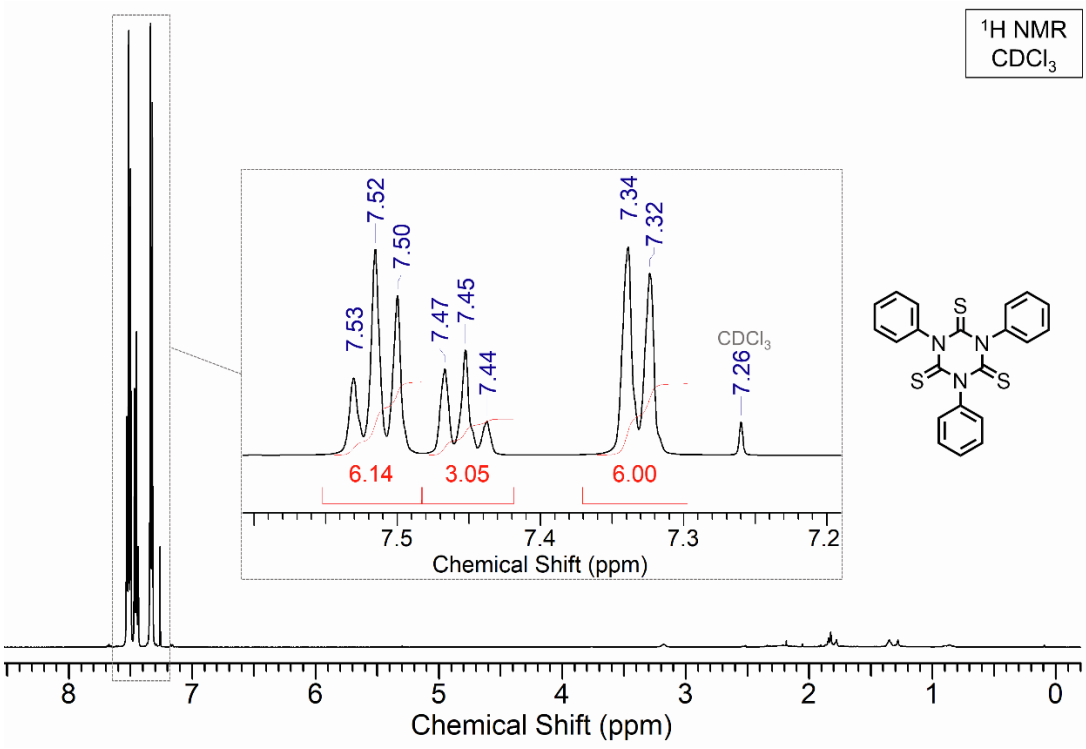

Figure S8. ^{1}H NMR (500 MHz, $CDCl_3$, 298 K) spectrum of Model Compound 1.

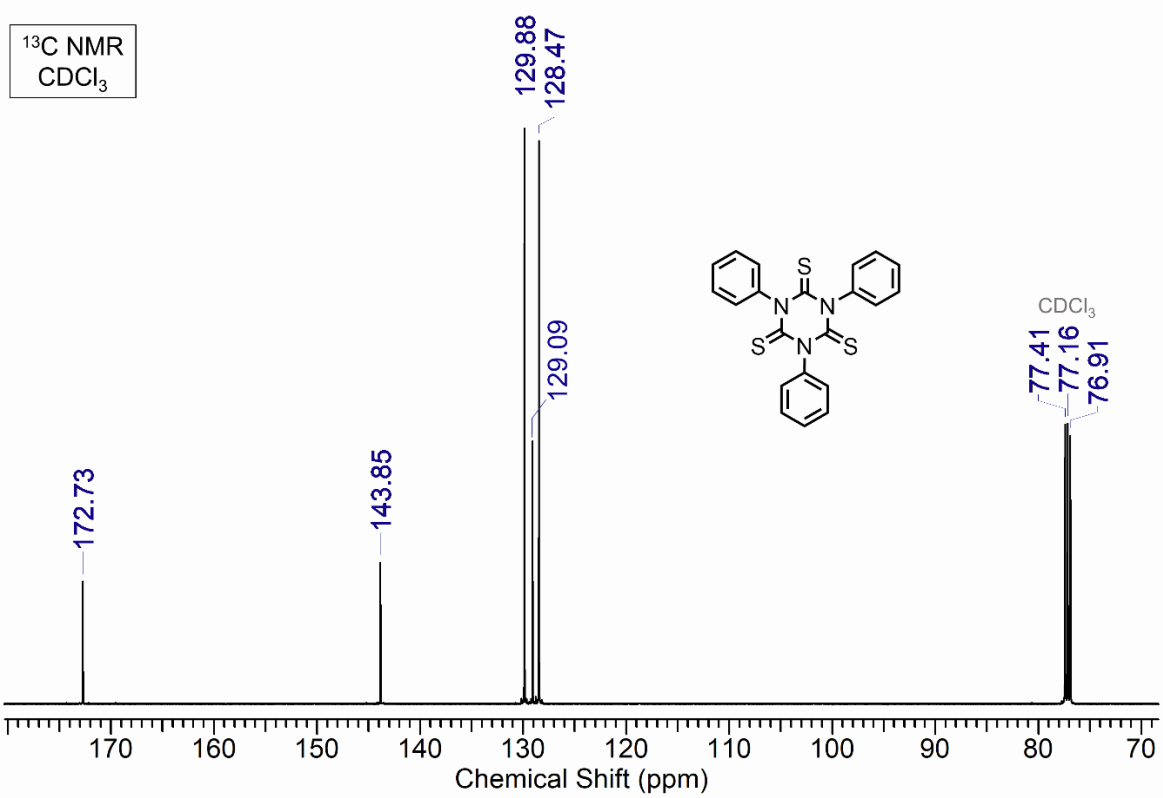

Figure S9. ^{13}C NMR (125 MHz, $CDCl_3$, 298 K) spectrum of Model Compound 1.

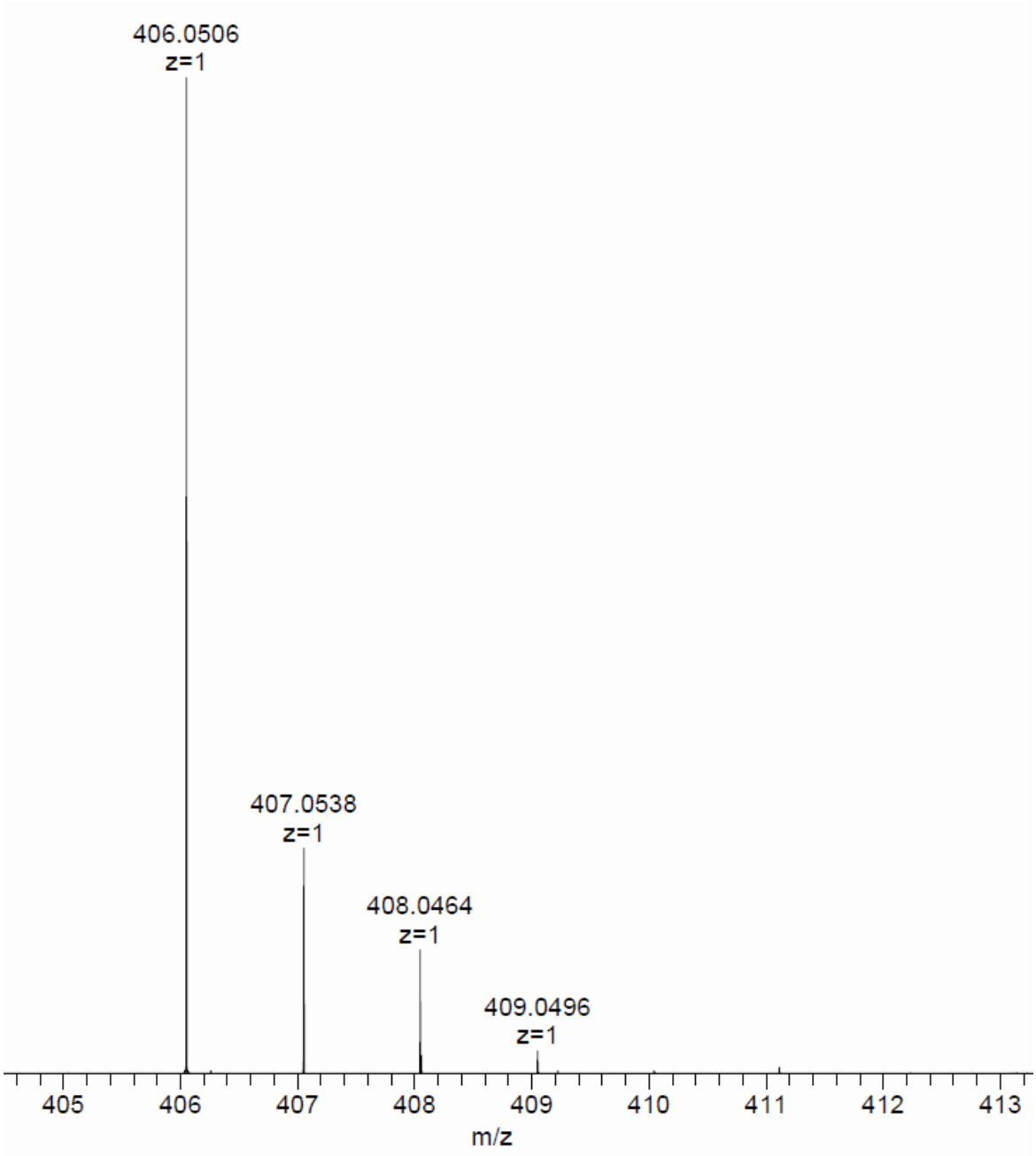

Figure S10. High-resolution mass spectrum (HRMS) of Model Compound 1.

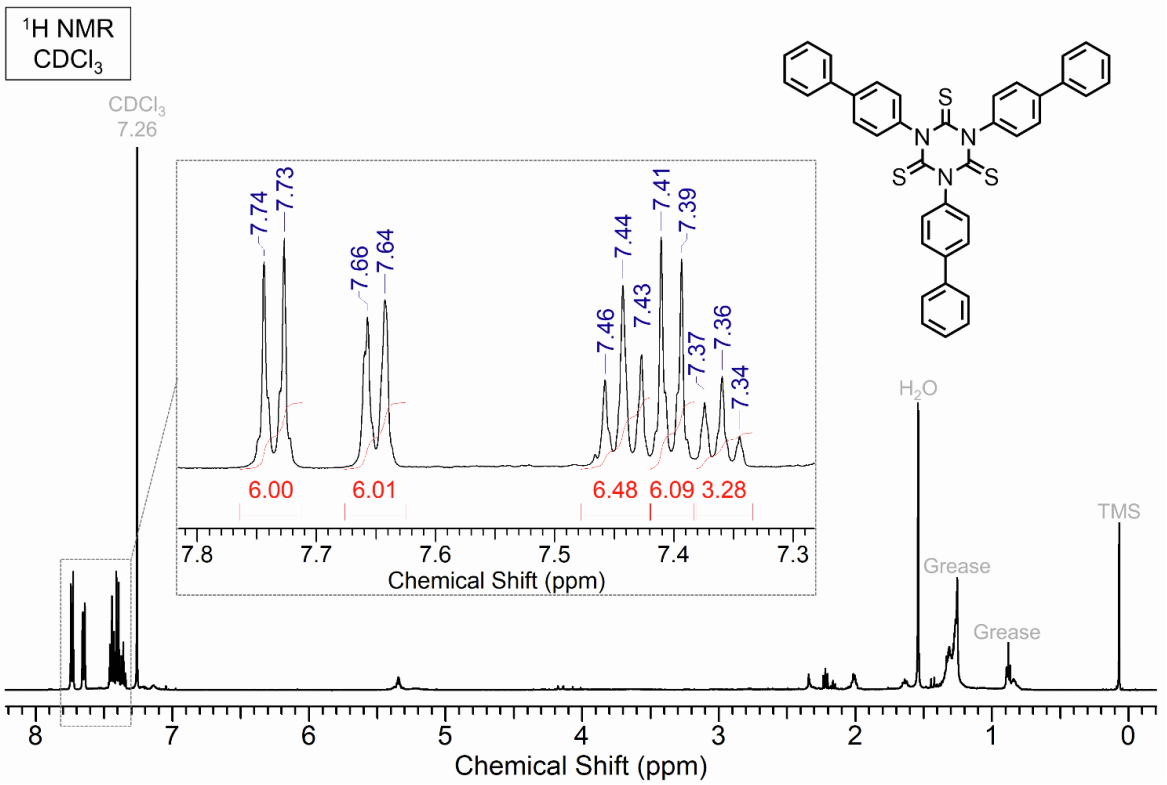

Figure S11. ^{1}H NMR (500 MHz, $CDCl_3$, 298 K) spectrum of Model Compound 2.

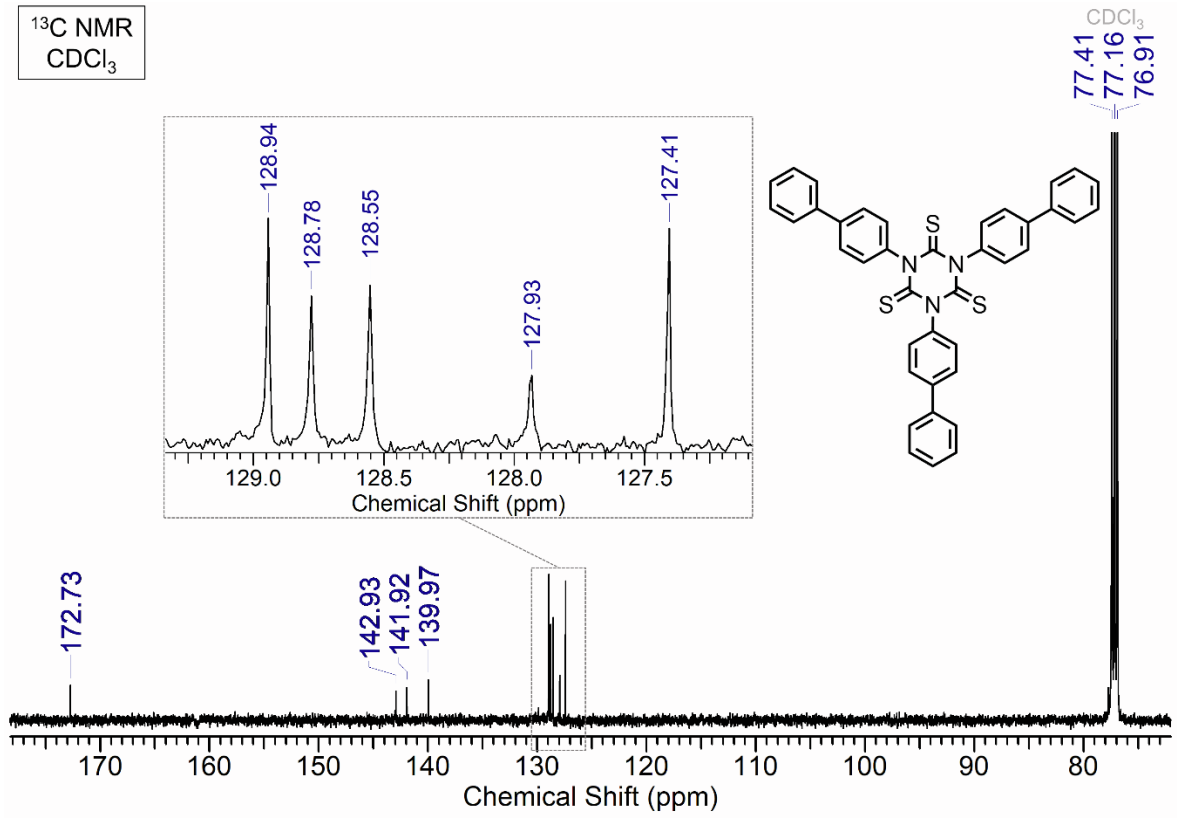

Figure S12. ^{13}C NMR (125 MHz, $CDCl_3$, 298 K) spectrum of Model Compound 2.

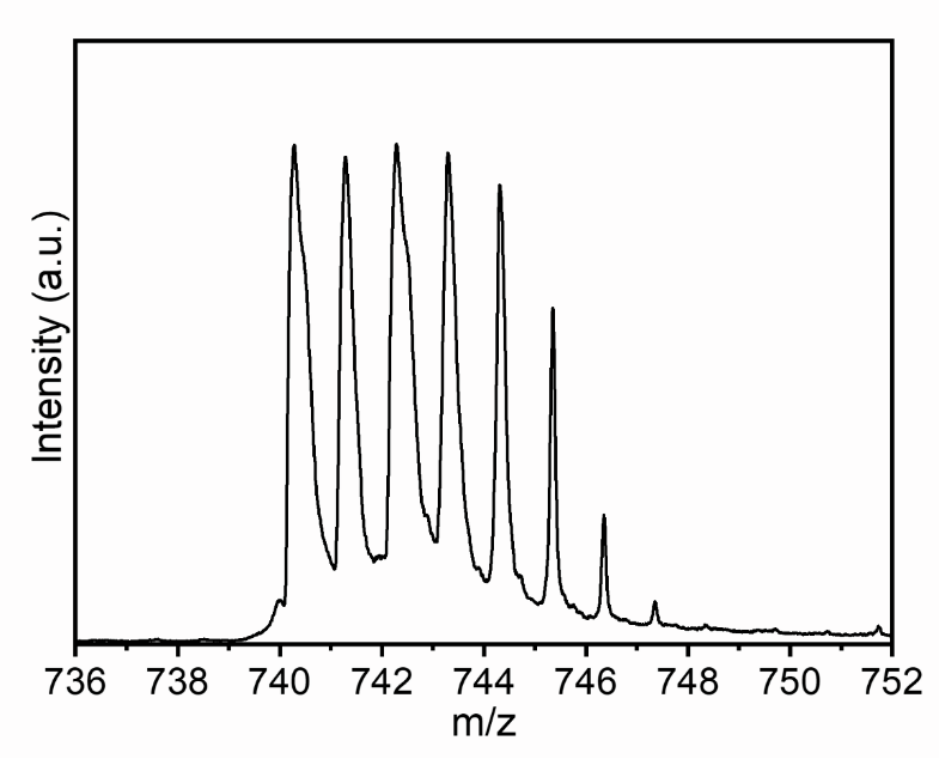

Figure S13. Matrix-assisted laser desorption/ionization (MALDI) analysis of Model Compound 2.

Note: All the further characterizations were performed for the samples synthesized using 5 eq. of $ZnCl_2$ due to their higher surface areas. Thus, the samples denoted as CITCF-3, CITCF-400 and CITCF-500 are for the samples synthesized at 300, 400 and 500°C , respectively.

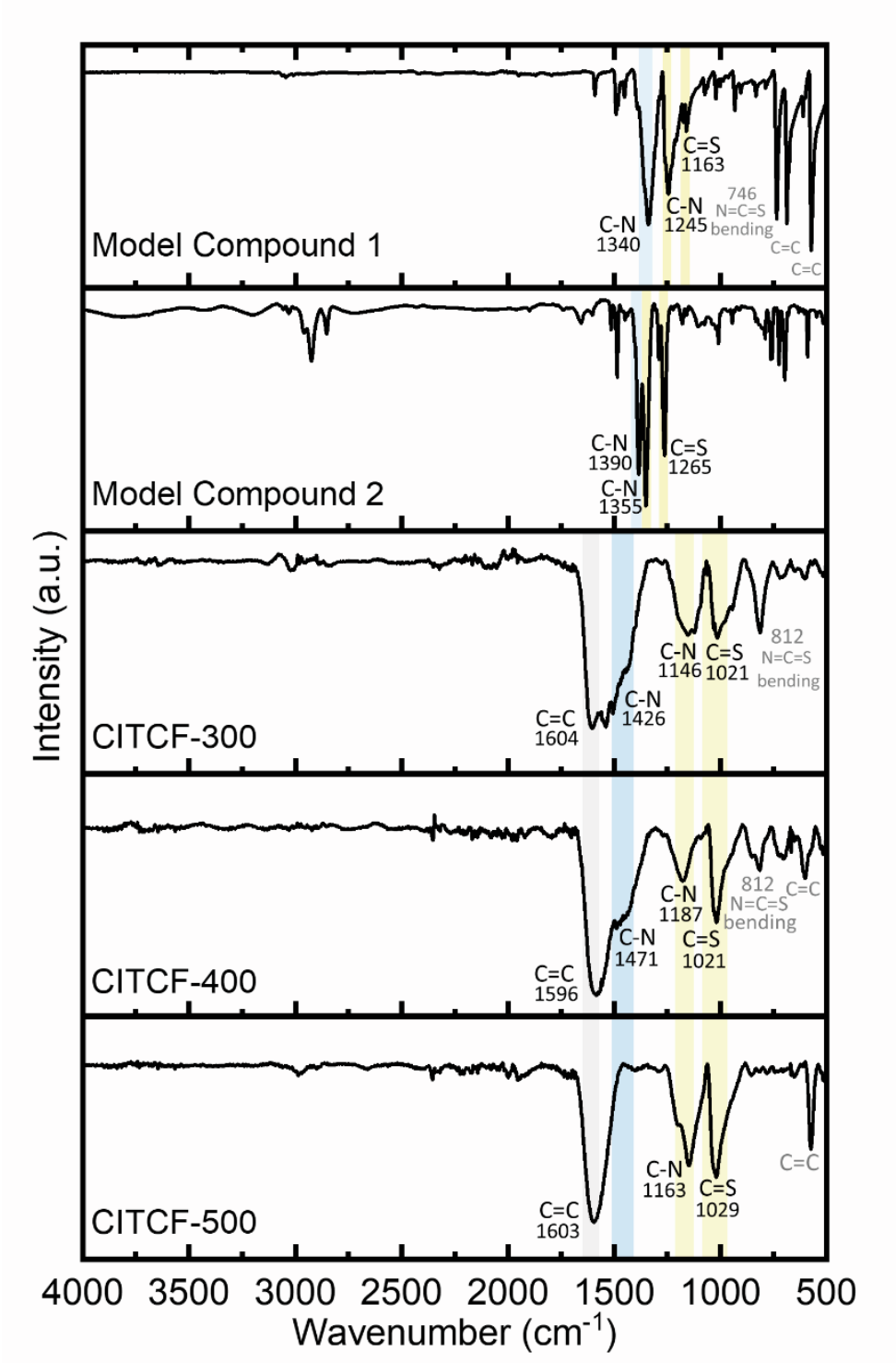

Figure S14. FT-IR analysis of model compound 1, model compound 2, CITCF-300, -400 and -500. Model compound 1 and 2 exhibited the three characteristic bands of thiocarbonyl derivatives (highlighted with blue and light-orange colors). CITCFs also showed these characteristic bands thus verifying the formation of isothiocyanurate linkages.

Table S3. Elemental analysis (EA) of CITCFs synthesized at different temperatures.

Sample	Elemental Analysis (wt%)				
	C	N	H	S	Total amount
	48.95 [a]	14.27 [a]	4.11 [a]	32.67 [a]	100
CITCF-5-300	50.6	13.5	1.5	18.0	83.6
CITCF-5-400	55.2	14.2	1.0	17.5	87.9
CITCF-5-500	58.0	14.6	0.6	13.9	87.1

[a] Theoretical elemental analysis (EA) value is calculated based on $C_{24}H_{24}N_6S_6$.

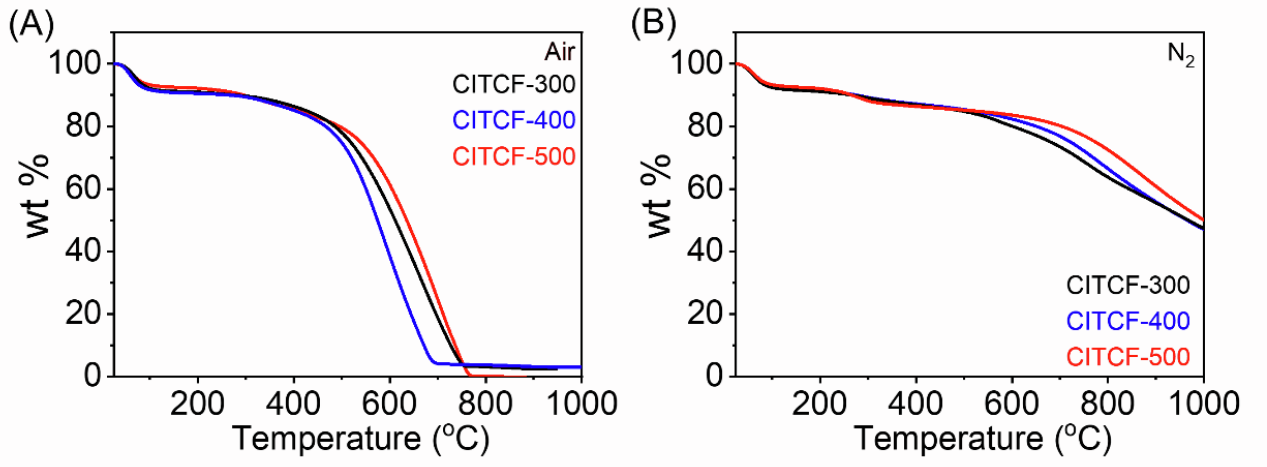

Figure S15. TGA curves of CITCFs. The thermal stability of CITCFs were assessed in the temperature range of 25 - 1000 °C under (A) air and (B) nitrogen atmosphere.

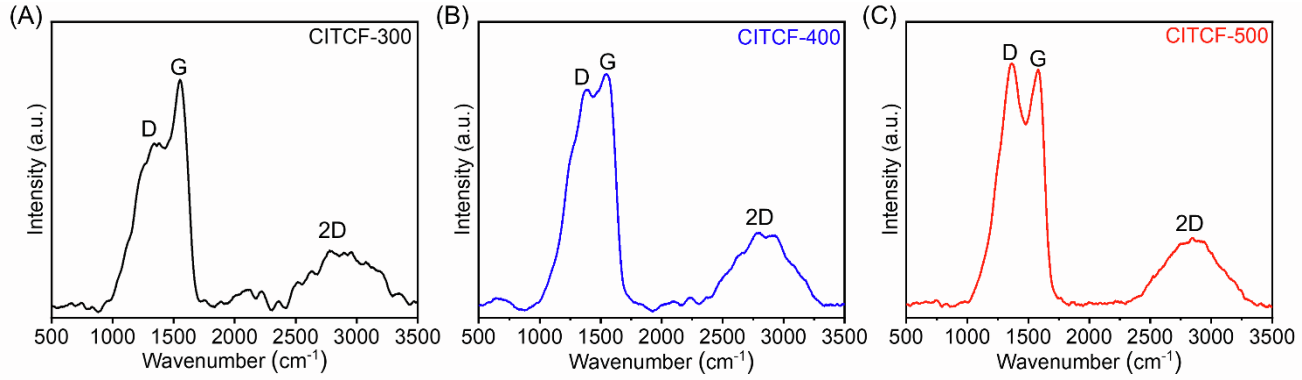

Figure S16. Raman analysis of CITCFs. Raman spectra of (A) CITCF-300, (B) CITCF-400 and (C) CITCF-500, which were measured using 532 nm laser source on powder samples.

Table S4. Raman analysis of CITCFs. The peak positions of D, G and 2D bands and the corresponding of I_D/I_G ratios.

	D band (cm^{-1})	G band (cm^{-1})	2D band (cm^{-1})	I_D/I_G
CITCF-300	1346.1	1546.5	2905.6	0.62
CITCF-400	1374.2	1550.6	2831.1	0.94
CITCF-500	1355.7	1569.0	2859.1	1.03

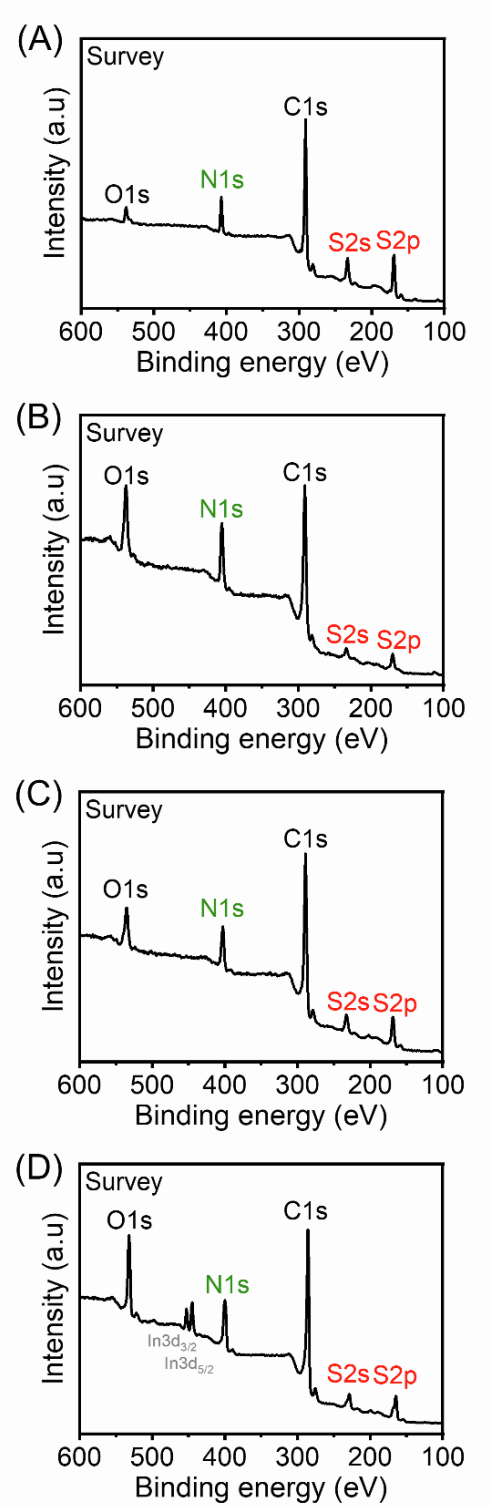

Figure S17. XPS analysis of model compound 1 and CITCFs. XPS Survey spectra of (A) Model Compound 1, (B) CITCF-300, (C) CITCF-400 and (D) CITCF-500. Indium holder was used for the analysis of CITCF-500, resulting in the observation of In3d peaks in the survey spectrum.

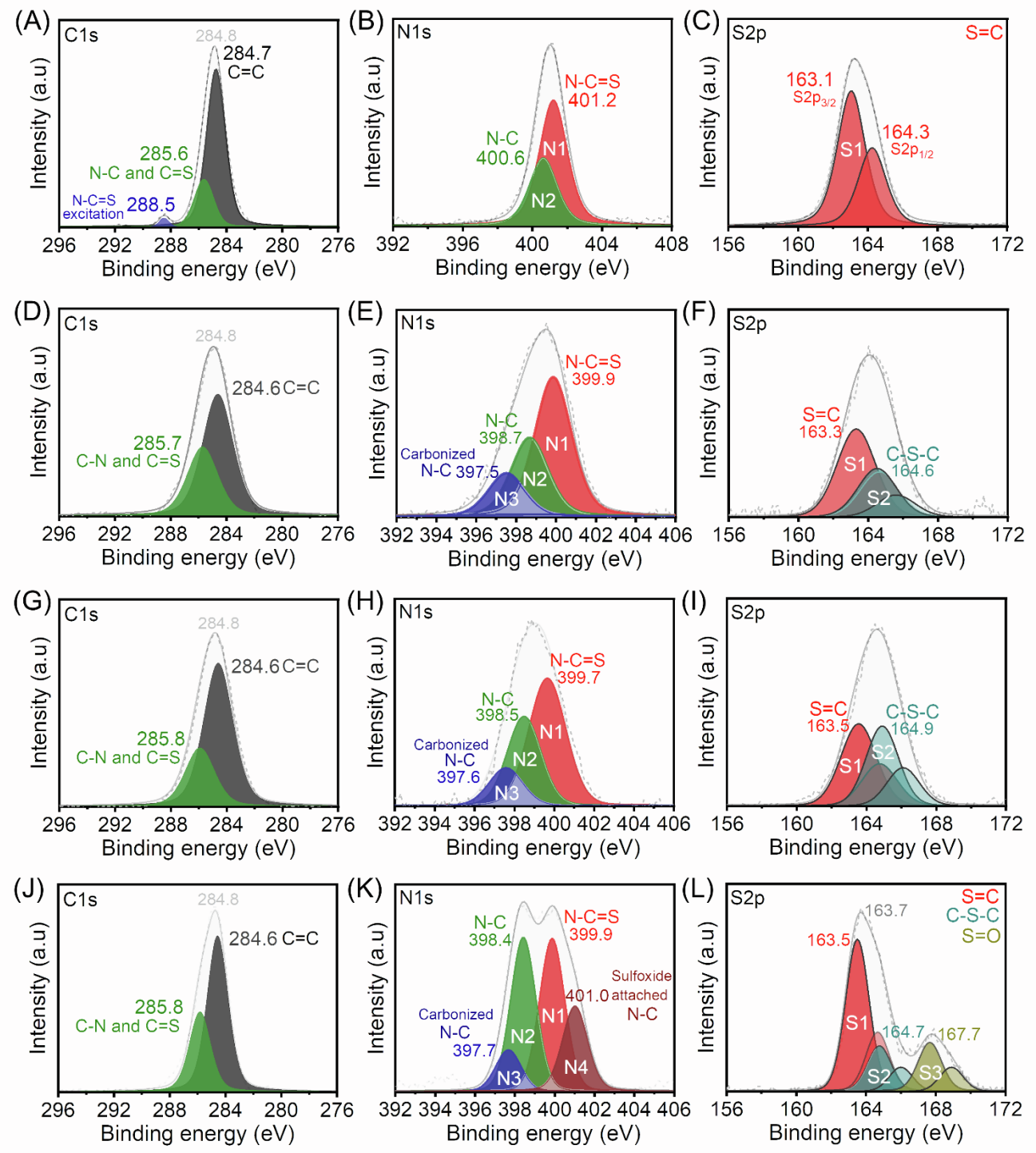

Figure S18. XPS analysis of model compound 1 and CITCFs. Deconvoluted XPS spectra of model compound 1 and CITCFs. (A) C1s, (B) N1s and (C) S2p of model compound 1. (D) C1s, (E) N1s and (F) S2p of CITCF-300. (G) C1s, (H) N1s and (I) S2p of CITCF-400. (J) C1s, (K) N1s, and (L) S2p of CITCF-500.

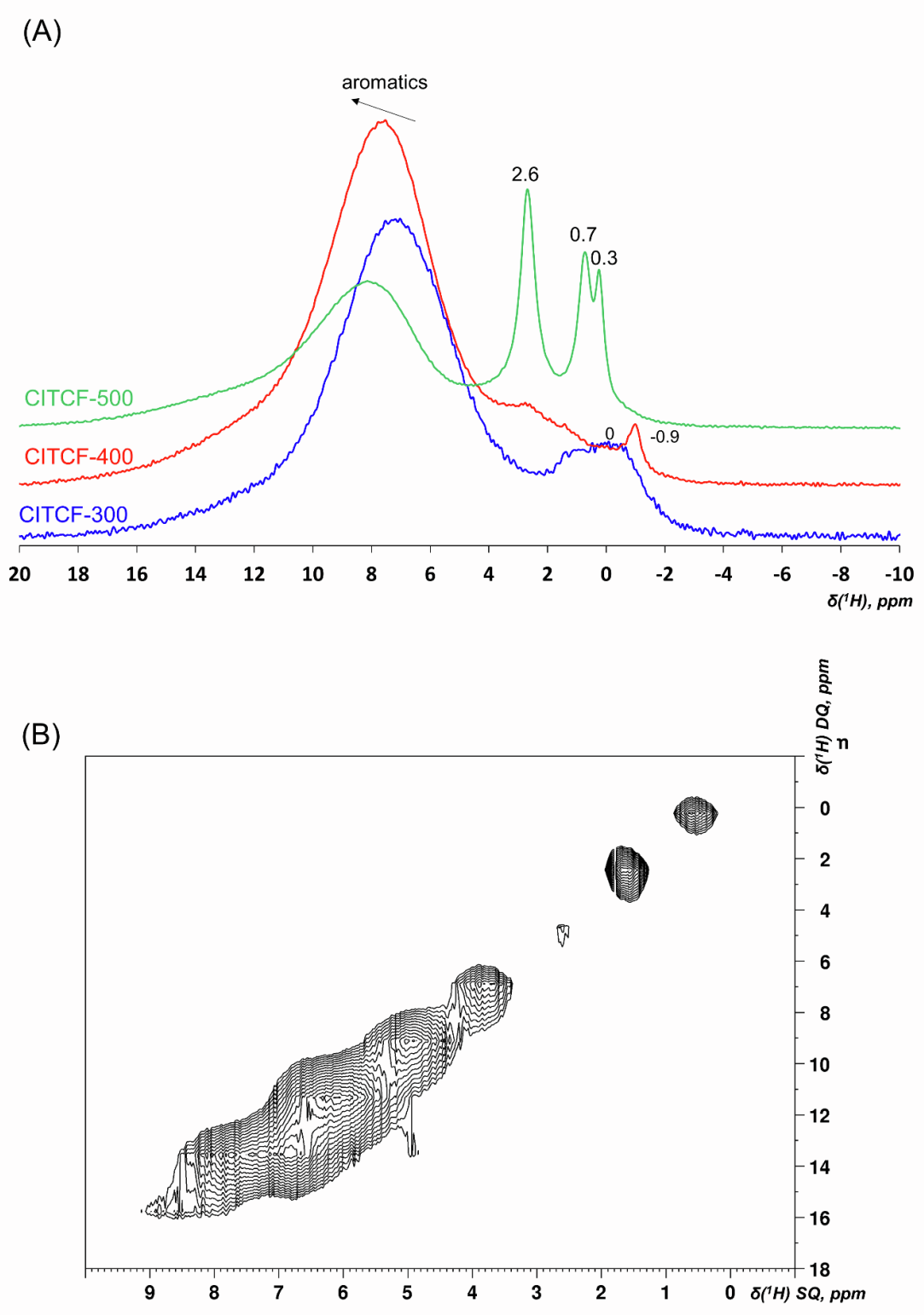

Figure S19. Solid State-NMR analysis. (A) ^{1}H MAS NMR spectra of CITCF-300, 400 and 500. (B) 2D ^{1}H single-quantum double-quantum (SQ-DQ) correlation NMR spectrum of CITCF-500.

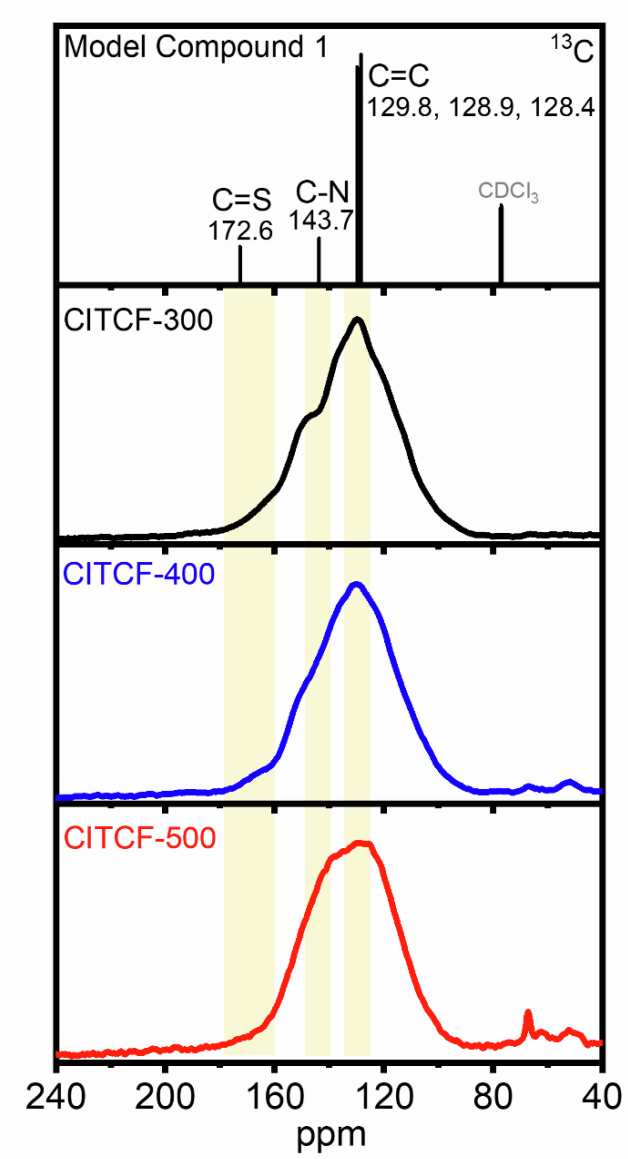

Figure S20. Solid State-NMR analysis. Comparison of the ^{13}C CP/MAS NMR spectra of CITCFs with the solution-state ^{13}C NMR spectrum (500 MHz, $CDCl_3$, 298 K) of Model Compound 1.

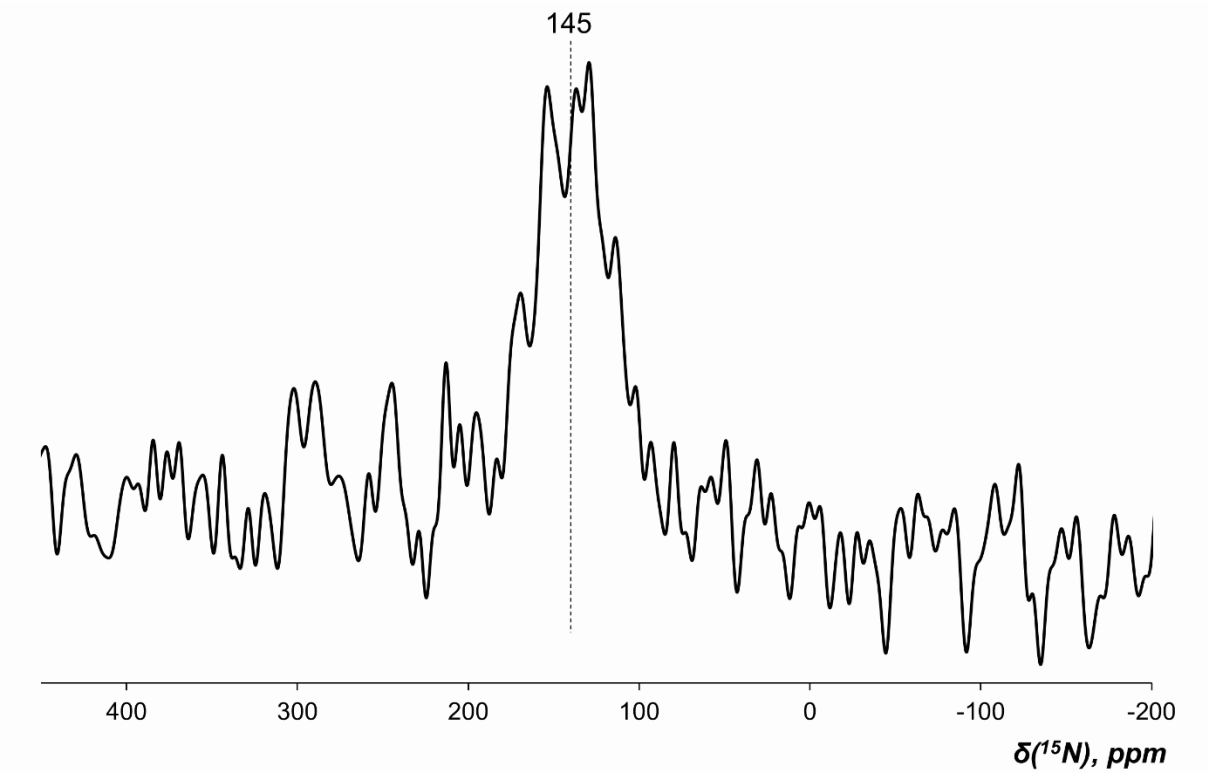

Figure S21. Solid State-NMR analysis. ^{15}N CP/MAS NMR spectrum (600 MHz, 100 K) of CITCF-500. The magic-angle spinning (MAS) rate was set to 8 kHz.

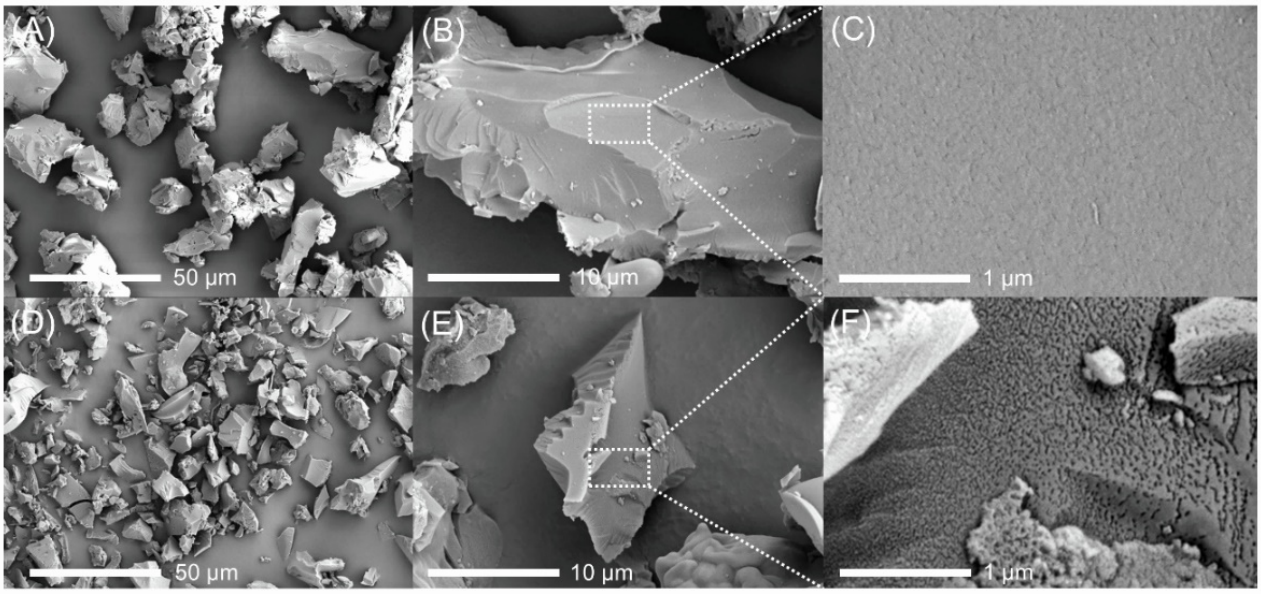

Figure S22. Morphology of CITCFs synthesized at different temperatures. SEM images of (A) CITCF-400, zoomed in regions (B), (C) and of CITCF-500 (D), zoomed in regions (E), (F)

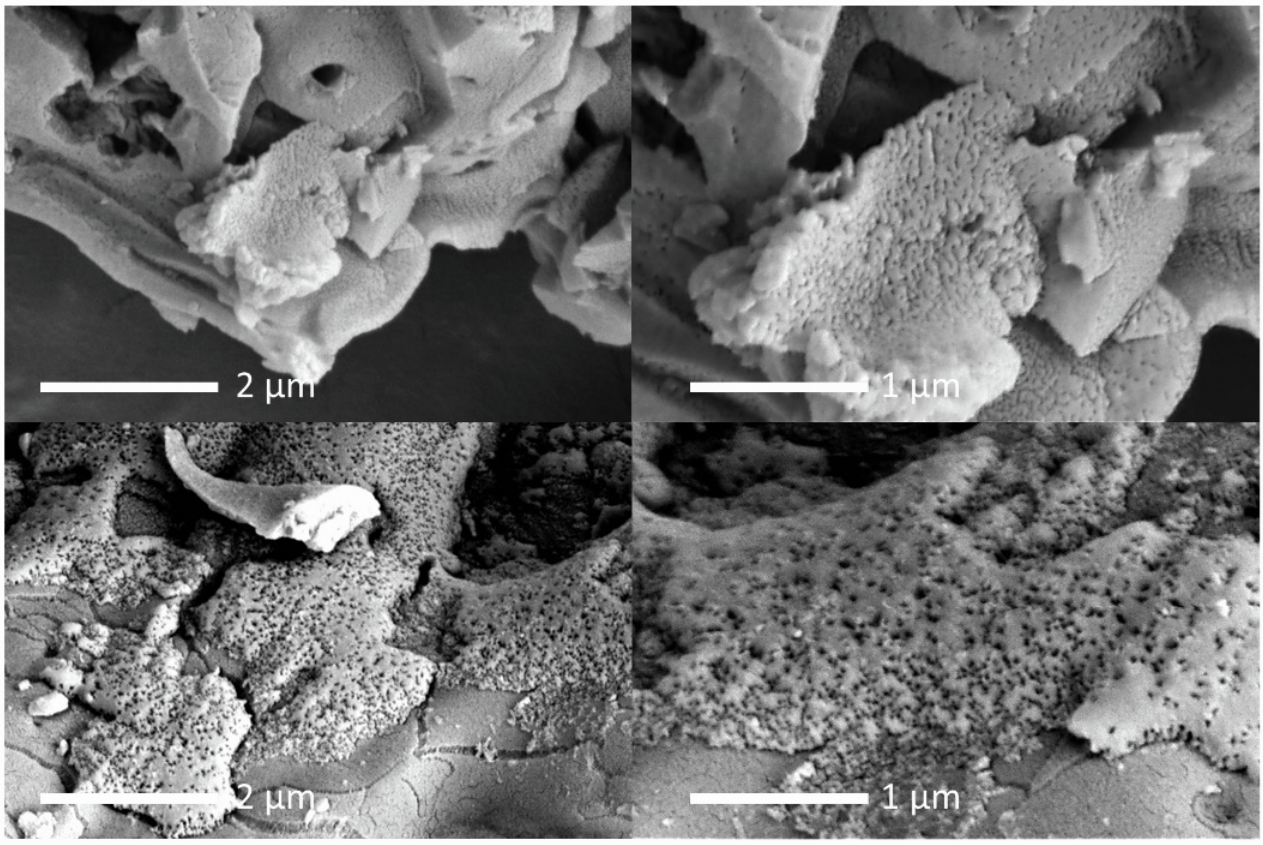

Figure S23. Expanded SEM micrographs of CITCF-500. From the SEM images, it can be observed that CITCF-500 has more defects.

Langmuir adsorption isotherm

$$q_e = \frac{Q_m k_l C_e}{1 + k_l C_e}$$

Q_m = Adsorption Capacity (constant)
k_L = Energy of Adsorption (constant)

Pd	Q_m (mg g^{-1})	k_l (L mg^{-1})
CITCF-500	909.1	0.101

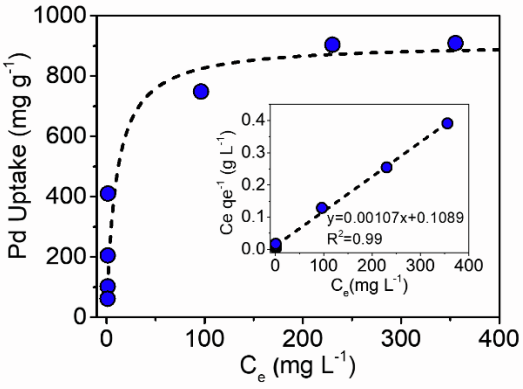

Figure S24. The fitting result of Pd(II) adsorption isotherm of CITCF-500. Fitting with the Langmuir adsorption model.

Freundlich isotherm

$$q_e = k_F C_e^{1/n}$$

k_F ,n = Freundlich constant

Pd	k_F (mg g^{-1})	n	R^2
CITCF-500	377.94	6.52	0.99

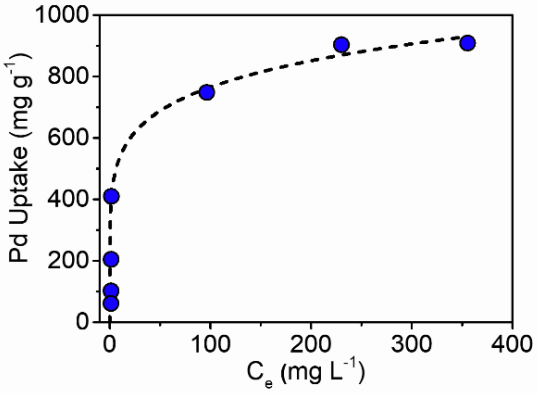

Figure S25. The fitting result of Pd(II) adsorption isotherm of CITCF-500. Fitting with the Freundlich isotherm model.

<Pseudo-second order model>

$$q_t = \frac{q_e^2 kt}{1 + q_e kt}$$

q_e (mg g^{-1}) = maximum equilibrium adsorption capacity
q_t (mg g^{-1}) = adsorption capacity at time t

	q_e (mg g^{-1})	k (g mg^{-1} min^{-1})	R
CICTCF-500	373.82	3.26 *10 ^{43}	100.0

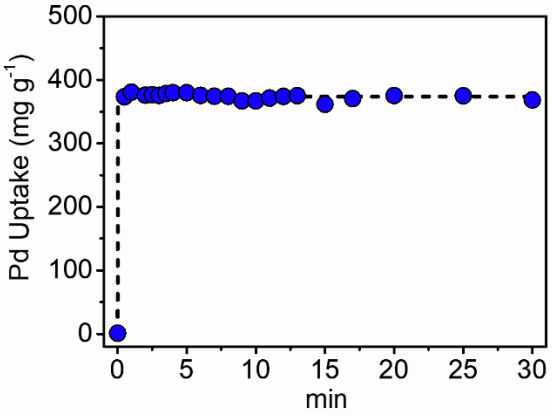

Figure S26. Pd(II) adsorption kinetic study. Pseudo-second order model was used for Pd adsorption kinetic of CITCF-500.

< Distribution coefficient (K_d) >

$$K_d = \frac{(C_0 - C_e)}{C_e} x \frac{V}{m}$$

- mg L^{-1} = ppm
- Co (mg L^{-1}) = Mother solution
- Ce (mg L^{-1}) = Equilibrium solution

	K_d (mL g^{-1})
CICTCF-500	5.6 * 10^5

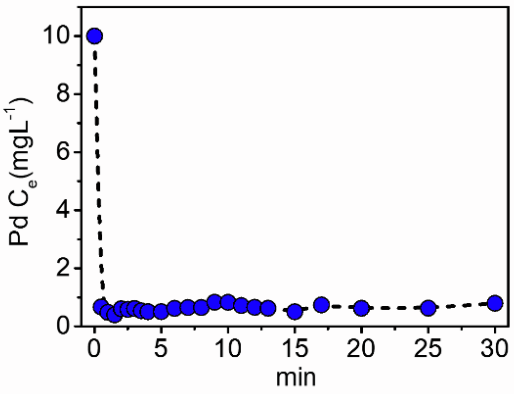

Figure S27. Pd adsorption kinetic study. The calculation of distribution coefficient (K_d) of CITCF-500.

Table S5. Pd Capture performance summary with previously reported Pd adsorbents.

	Sample	Binding Motif	Binding	BET (m^2g^{-1})	Maximum Pd Uptake (mg g^{-1}) [a]	k (g mg^{-1} min^{-1}) [b]	Kd (mL g-1) [c]	REF
1[d]	CITCF-500	Trithiocyanurate ring	Pd-S	1589	909.1	3.26×10^{43}	5.6×10^5	This work
2[d]	POP-oNH_2-Py	o-NH_2-Pyridine	Pd-N (pyridine) Pd-Cl-HN (o-amine)	359	752	-	1.1×10^8	1
3[d]	COP-214	Pyrazole	Pd-N	308	103	-	-	2
4[d]	CPTPN-Cl	Cationic pyridyl trizaine	Pd-N	384	339.8	0.0208	-	3
5[e]	MOF-802	Zr-oxo-cluster	Pd-Cl-Zr	4.8	25.8	0.048	-	4
6[e]	MOF-808	Zr-oxo-cluster	Pd-Cl-Zr	1314	163.9	4.159	-	4
7[e]	UiO-66	Zr-oxo-cluster	Pd-Cl-Zr	1507	105.1	9.518	-	4
8[e]	UiO-66-NH_2	Zr-oxo-cluster and amine	Pd-Cl-NH_3^+	1067	167	-	-	5
9	Thiourea-form aldehyde	Thiourea	Pd-S Pd-N	-	31.85	-	-	6
10	TCS	Thiourea	Pd-S	95.6	112.4	5.05×10^{-4}	-	7
11	Chitosan-MBI	Mercaptobenimidazol	$(RNH_3^+)_2PdCl_4^{2-}$ Pd-S, Pd-N	-	19.26	0.255	-	8
12	Cellulose-MBT	Mercaptobenzothiazole	Pd-S, Pd-N, Pd-O	-	5.00	0.4576	-	9
13	Thio-SBA-15	Thiol	Pd-S	437	10.43	-	-	10
14	TRIS	Tris (2-Aminoethyl) Amine	$PdCl_2N_2^{2-}$	-	187.5	0.00001	-	11
15	β-cyclodextrin grafted chitosan	Cyclodextrine and amine	Pd-O Pd-N	-	202.02	0.0508	-	12
16	PEI-chitin	Polyethyl amine	$(RNH_3^+)_2PdCl_4^{2-}$	389.42	872.1	0.0056	-	13
17	Triazine polymer (TAPEHA)	Triazine and Amine	Pd-N	10.981	465	0.001	-	14
18	Chitosan-Crownether (Chitosan-DB18C6)	Crownether	Pd-O	14.44	20.3	0.05022	-	15
19	Crownether function-alized Silica	Crownether	Pd-O	72	83.0	0.0173	-	16

20	LMCCR (crosslinked chitosan resin)	Crosslinked chitosan resin	$(RNH_3^+)_2PdCl_4^{2-}$	82.4	109.47	0.0185	-	[17]
21	Activated Carbon	-	Pd-pi interaction	922.33	35.71	0.103	-	[18]
22	Graphene Oxide	-	Pd-pi interaction Pd-O (C=O)	-	80.775	0.000506	-	[19]
23	Mesoporous Silica-MBHB	Methoxycarbonyl ligand	Pd-O	466	184.50	-	-	[20]
24	PEI-AO (Alumina)	Polyethylene amine	Pd-N	155	97.7	0.1004	-	[21]

[a] Calculated with the Langmuir Adsorption Model. [b] Pseudo-second Order Model. [c] Distribution Coefficient [d] Porous Organic Polymers (POPs) [e] Metal Organic Frameworks (MOFs)

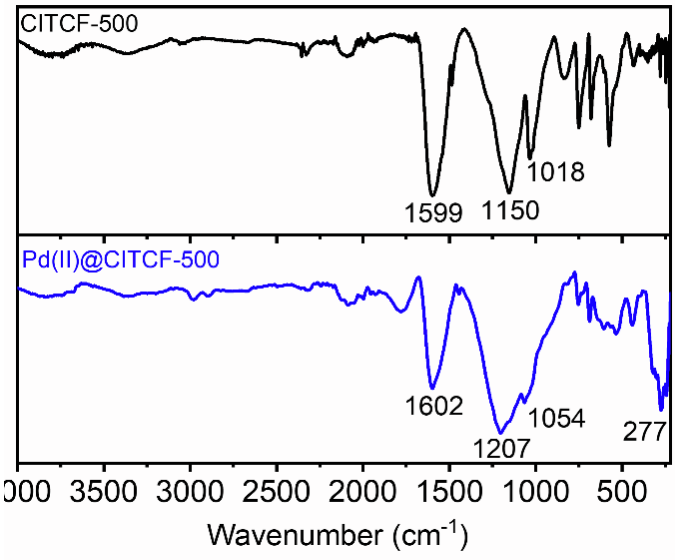

Figure S28. Chemical characterization of CITCF-500 before and after Pd(II) uptake. FTIR spectrum of CITCF-500 (top) and Pd^{2+}@CITCF-500 (bottom). Here the formation of Pd-S coordination bond can be clearly seen at 277 cm^{-1}. Additionally, band shifts of trithiocyanurate ring (from 1599 to 1602 cm^{-1} and from 1150 to 1207 cm^{-1}) also confirm Pd(II) binding.

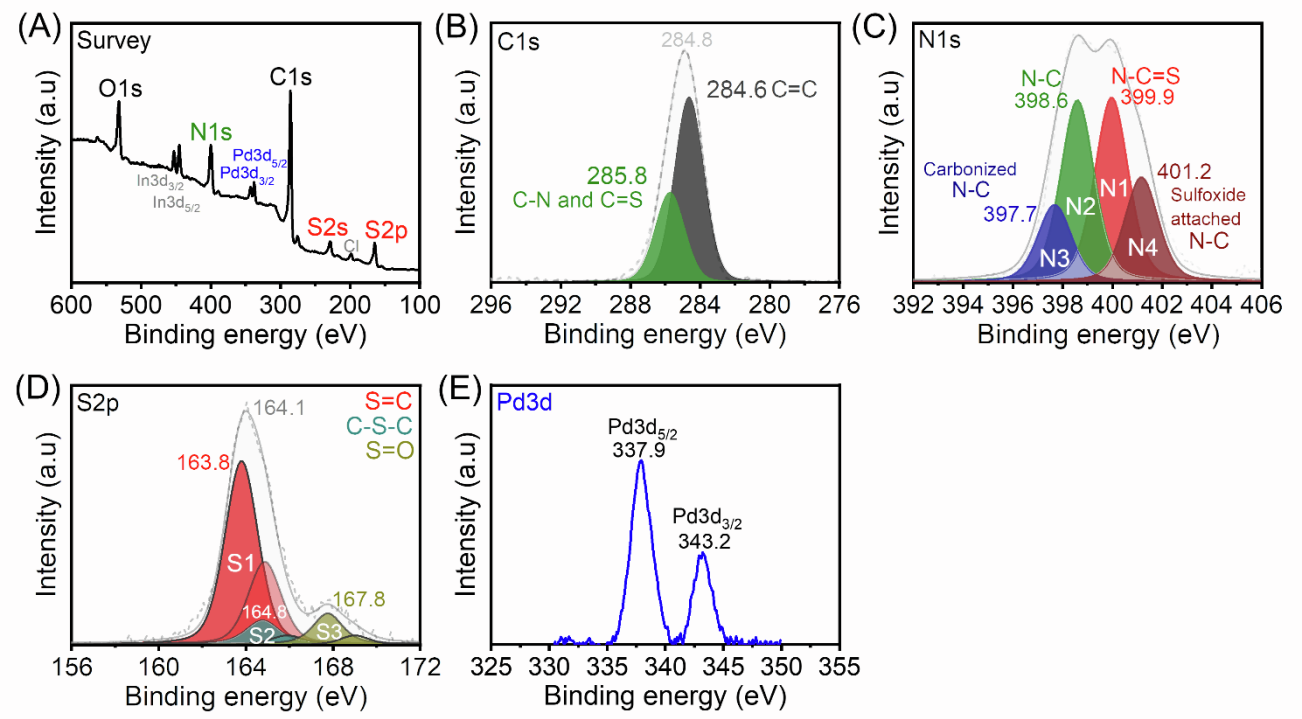

Figure S29. XPS analysis of Pd(II)@CITCF-500. (A) XPS survey spectrum and the deconvoluted (B) C1s (C) N1s (D) S2p (E) Pd3d spectra of Pd(II)@CITCF-500.

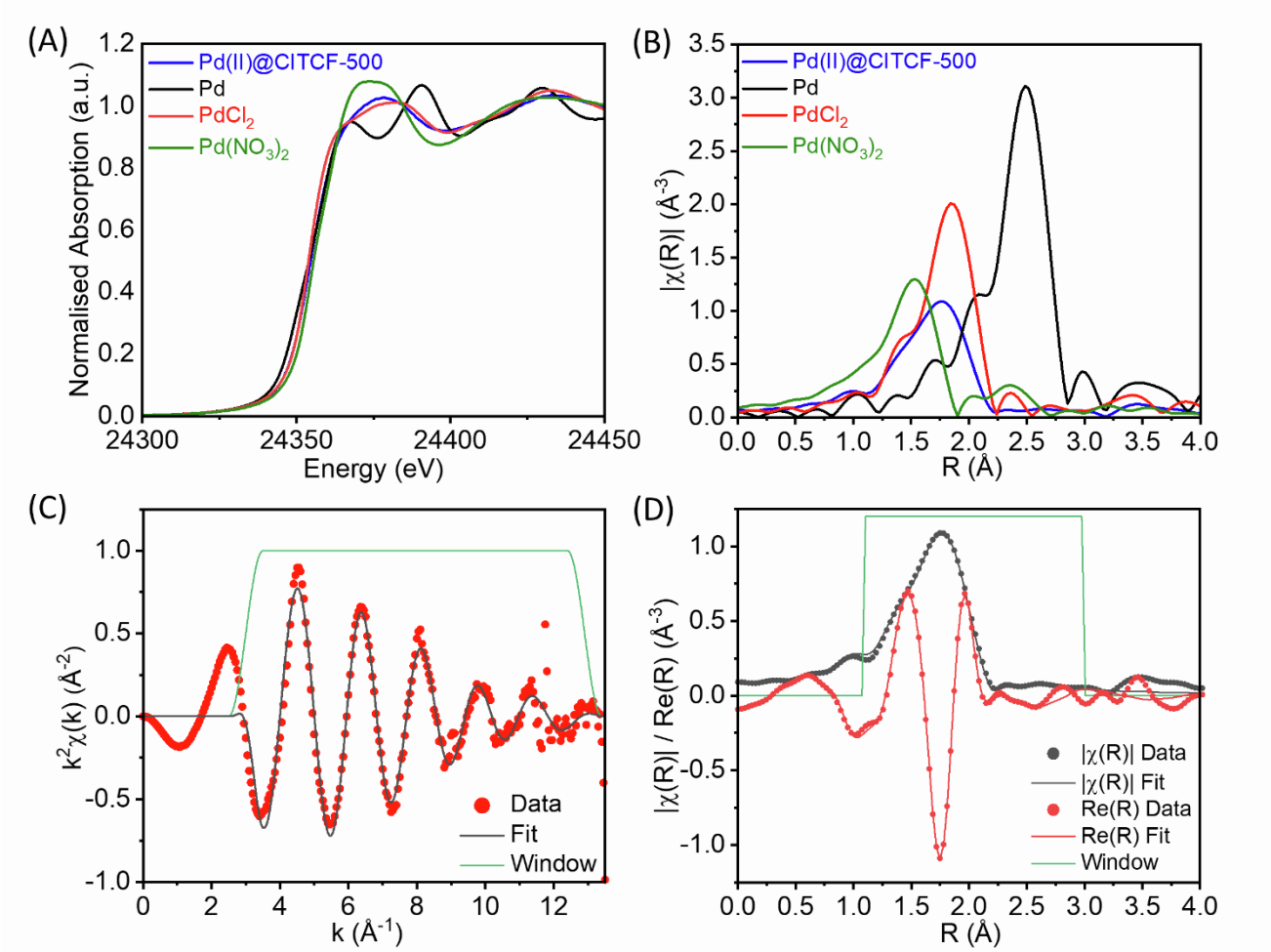

Figure S30. Extended X-ray Absorption Fine Structure (EXAFS) of Pd(II)@CITCF-500. (A) Pd-K edge EXAFS for comparison of Pd(II)@CITCF-500 and palladium reference chemicals. (B) k^2-weighted Fourier transform of the EXAFS function for Pd(II)@CITCF-500 (C), (D) Fitting EXAFS result of Pd(II)@CITCF-500 with a combination of Pd-S and Pd-O interaction mode.

Table S6. The EXAFS fitting results of Pd(II)@CITCF-500 with Pd-S and Pd-O mode.

Scattering path	S02	N	σ2 (Å2)	e0 (eV)	R (Å)
Pd-S	0.880	2.9 ± 0.3	0.0058 ± 0.001	1.5	2.31 ± 0.01
Pd-O	0.880	0.8 ± 0.2	0.0025 ± 0.001	1.5	2.05 ± 0.02

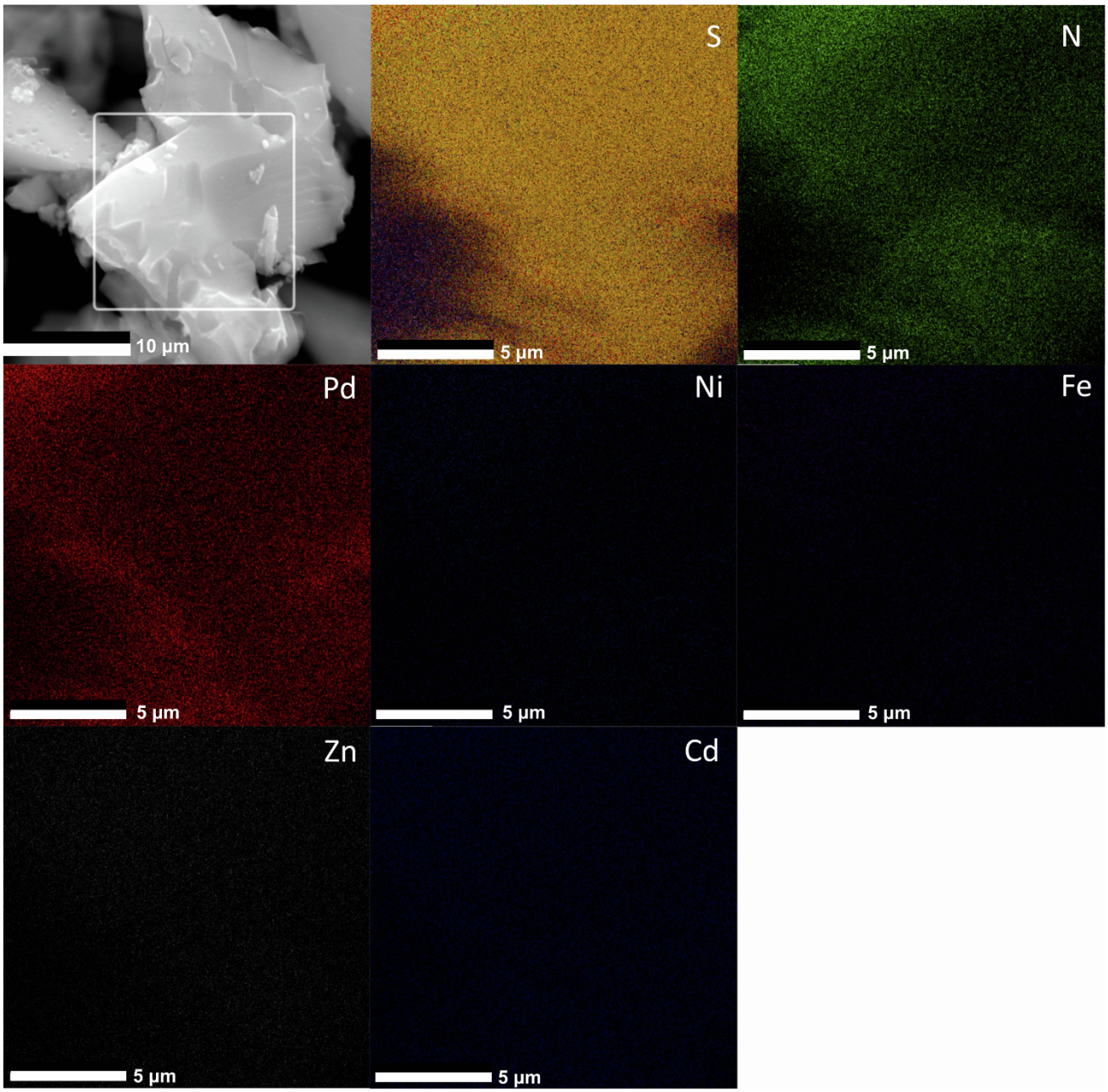

Figure S31. Energy-dispersive X-ray spectroscopy (EDX) analysis of CITCF-500 after selective Pd(II) capture from waste water conditioned metal mixture solution. EDX mapping of S, N, Pd, Ni, Fe, Zn and Cd. We observed high intensity and homogeneous distribution of Pd and the absence of other transition metals.

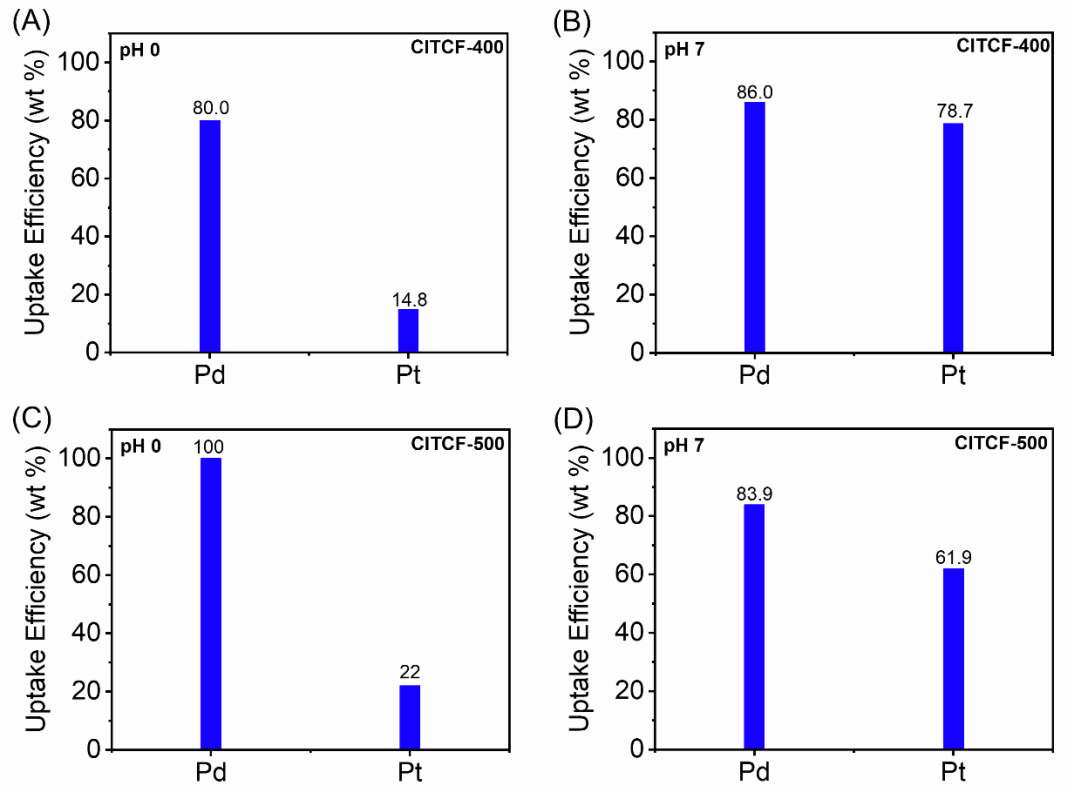

Figure S32. Pd/Pt selectivity of CITCFs using 5 ppm Pd and Pt mixture solution. Selective Pd capture at pH 0 and pH 7 of (A), (B) CITCF-400 and (C), (D) CITCF-500. CITCFs showed higher Pd(II) uptake efficiency compared to Pt(IV).

<Pseudo-second order model>

$$q_t = \frac{q_e^2 kt}{1 + q_e kt}$$

q_e (mg g^{-1}) = maximum equilibrium adsorption capacity
q_t (mg g^{-1}) = adsorption capacity at time t

	q_e (mg g^{-1})	k (g mg^{-1} min^{-1})	R
CICTCF-500	344.96	0.00734	100.0

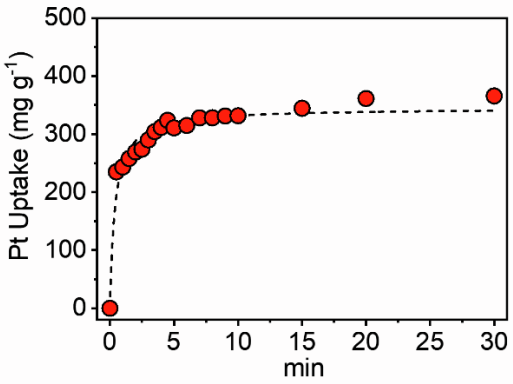

Figure S33. Pt(IV) adsorption kinetic study. Pseudo-second order model was used for Pt(IV) adsorption kinetic of CITCF-500.

< Distribution coefficient (K_d) >

$$K_d = \frac{(C_o - C_e)}{C_e} x \frac{V}{m}$$

- mg L^{-1} = ppm
- Co (mg L^{-1}) = Mother solution
- Ce (mg L^{-1}) = Equilibrium solution

	K_d (mL g^{-1})
CICTCF-500	5.7 * 10^4

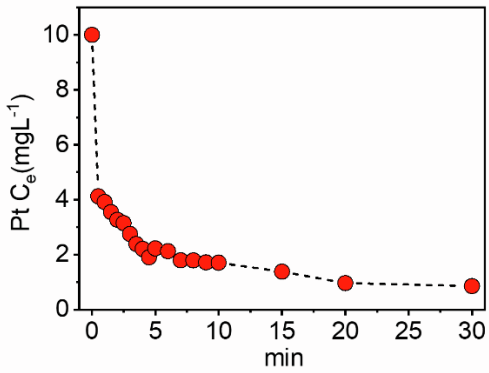

Figure S34. Pt(IV) adsorption kinetic study. The calculation of distribution coefficient (K_d) of Pt(IV).

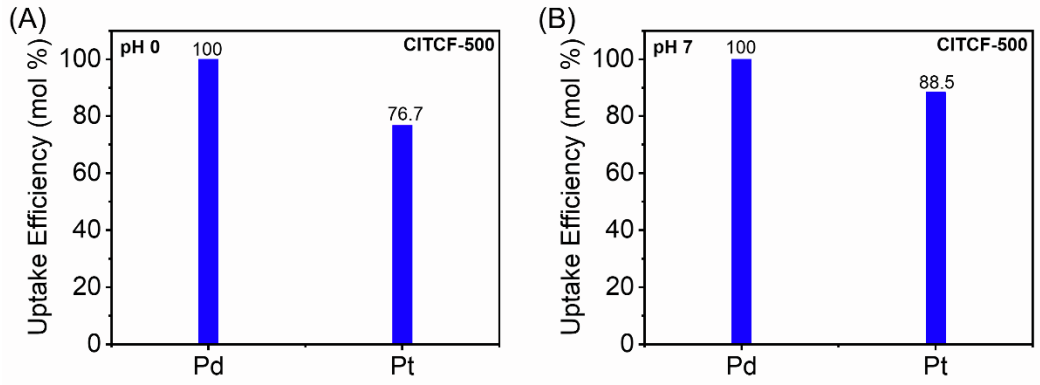

Figure S35. Pd(II)/Pt(IV) selectivity of CITCF-500 for equimolar (0.05 mM) mixture of Pd(II) and Pt(IV).

Table S7. Catalytic performance of Pd(II)@CITCF-500 in the Suzuki Miyaura cross coupling reaction.

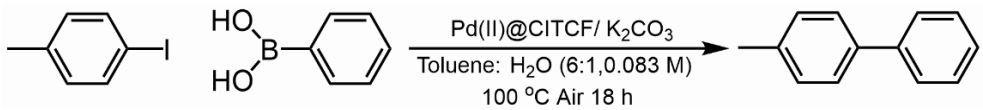

	Catalyst [a] (Pd mol %)	4-Iodo toluene (mole eq)	Phenyl boronic acid (mole eq)	K_2CO_3 (mole eq)	Conversion [b] (%)	Selectivity (%) [b] Ph-Ph-CH_3	H_3C-Ph-Ph-CH_3
1	9	1	1.5	1	13.0	99.0	1.0
2	9	1	1.5	3	99.9	10.0	90.0
3	9	1	1.5	6	72.0	71.1	28.9

[a] 10 mg Pd(II)@CITCF-500 (containing 450 mg/g Pd) was used as a catalyst.

[b] Calculated from GC-MS data.

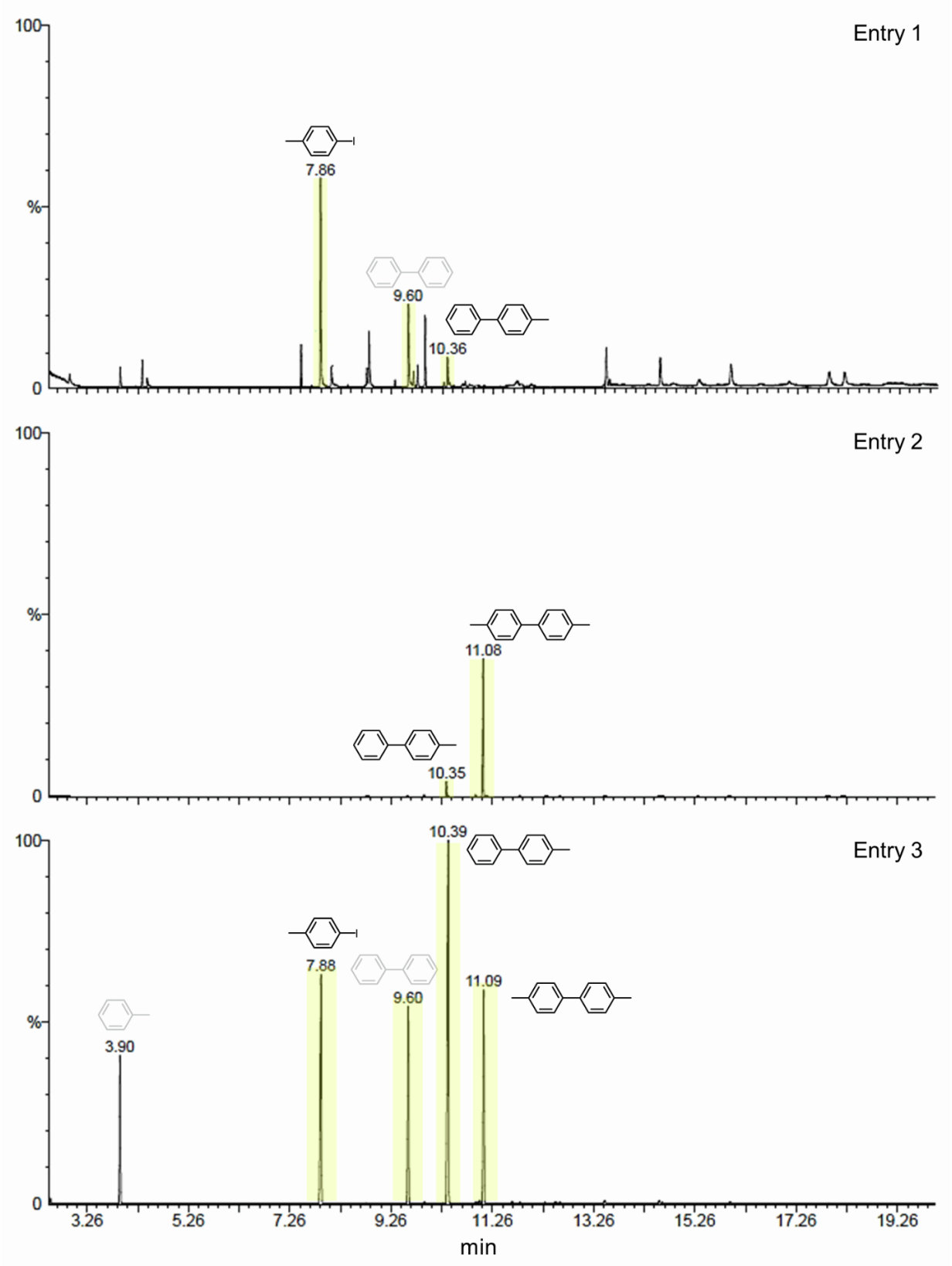

Figure S36. Suzuki Miyaura cross coupling reactions catalyzed by Pd(II)@CITCF-500. GC analysis of entry 1-3 of Table S7The corresponding peaks of reactants and products are highlighted in yellow on the chromatograms.

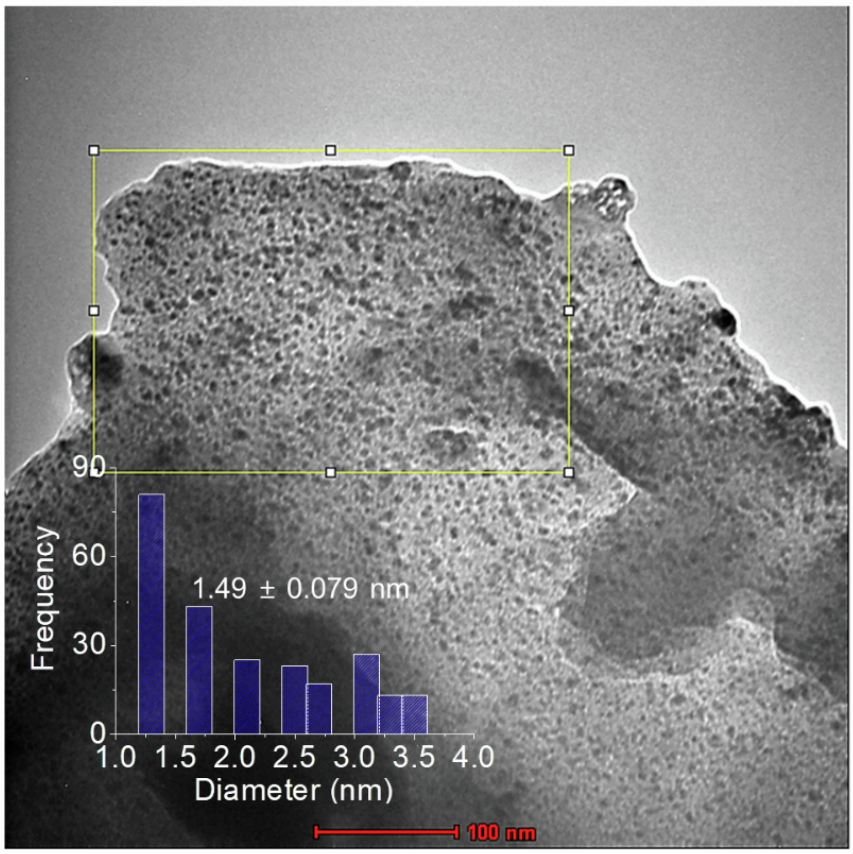

Figure S37. Morphology analysis of Pd@CITCF-500. TEM image shows average size of 1.49 nm Pd nanoparticle (Pd NPs) after the reduction.

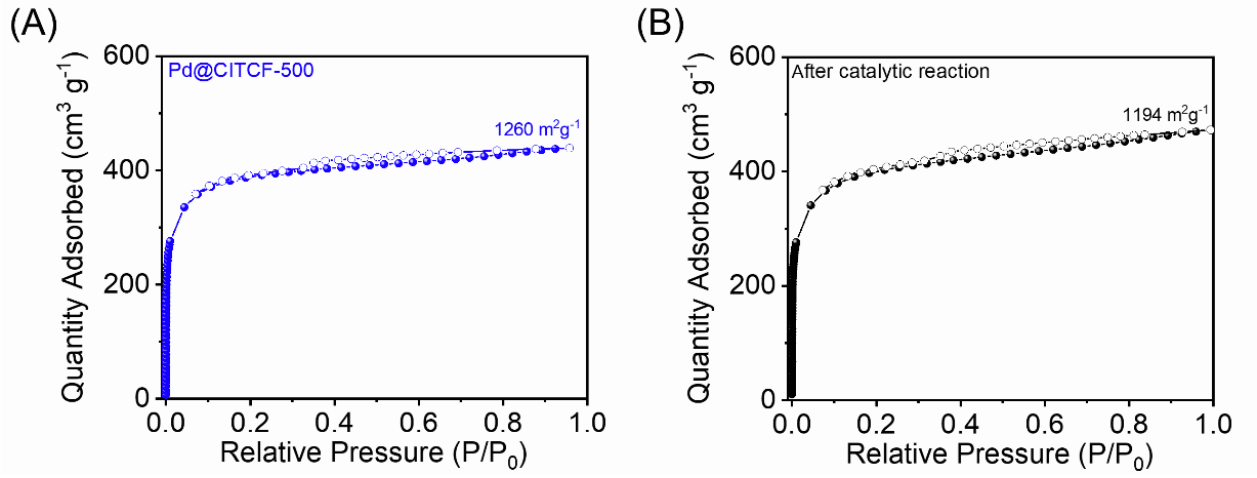

Figure S38. Surface area analysis Pd@CITCF-500 before and after catalytic tests. BET surface area analysis of (A) freshly prepared Pd@CITCF-500 and (B) Pd@CITCF-500 after five catalytic cycles (4-amino-bromobenzene and phenyl boronic acid, entry 4 in Table 2).

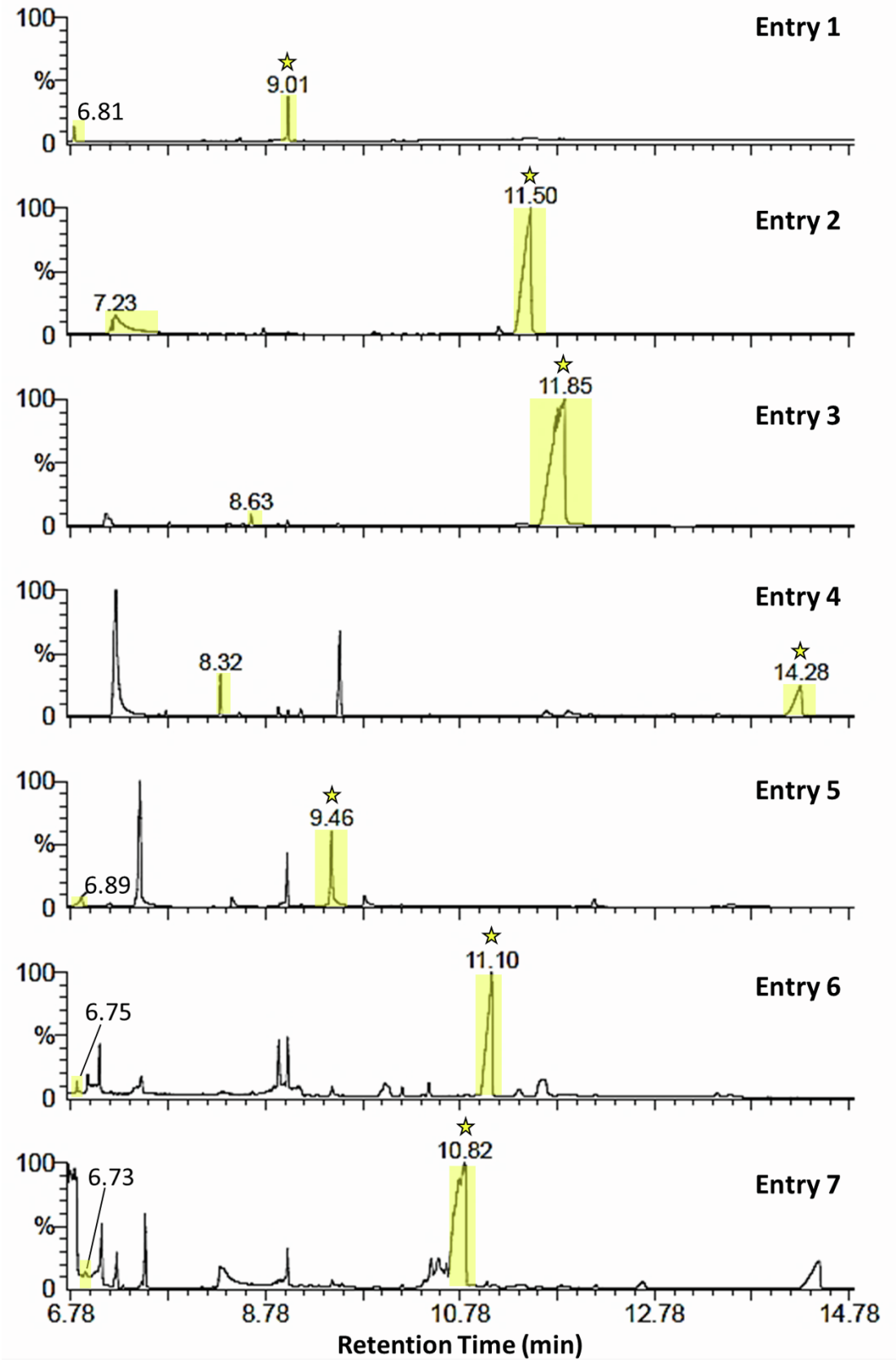

Figure S39. Suzuki Miyaura cross coupling reactions catalyzed by Pd@CITCF-500. GC analysis of entry 1-7 of Table 2. The corresponding peaks of reactants and products are highlighted in yellow on the chromatograms.

Supplemental References

1. Aguila, B., Sun, Q., Cassady, H. C., Shan, C., Liang, Z., Al-Enizic, A. M., Nafadyc, A., Wright, J. T., Meulenberg, R. W. & Ma, S. (2020). A Porous Organic Polymer Nanotrap for Efficient Extraction of Palladium. Angew. Chem. Int. Ed. *132*, 19786-19790. https://doi.org/10.1002/anie.202006596.

2. Garai, M., Mahato, M., Hong, Y., Rozyyev, V., Jeong, U., Ullah, Z. & Yavuz, C. T. (2021). Asynchronous Double Schiff Base Formation of Pyrazole Porous Polymers for Selective Pd Recovery. Adv. Sci., 2001676. https://doi.org/10.1002/advs.202001676.

3. Yuan, X., Wang, Y., Wu, P., Ouyang, X., Bai, W., Wan, Y., Yuan, L. & Feng, W. (2022). High acidity-and radiation-resistant triazine-based POPs for recovery of Pd (II) from nuclear fission products. Chem. Eng. J. *430*, 132618. https://doi.org/10.1016/j.cej.2021.132618.

4. Lin, S., Zhao, Y., Bediako, J. K., Cho, C.-W., Sarkar, A. K., Lim, C.-R. & Yun, Y.-S. (2019). Structure-controlled recovery of palladium (II) from acidic aqueous solution using metal-organic frameworks of MOF-802, UiO-66 and MOF-808. Chem. Eng. J. *362*, 280-286. https://doi.org/10.1016/j.cej.2019.01.044.

5. Lin, S., Reddy, D. H. K., Bediako, J. K., Song, M.-H., Wei, W., Kim, J.-A. & Yun, Y.-S. (2017). Effective adsorption of Pd (ii), Pt (iv) and Au (iii) by Zr (iv)-based metal–organic frameworks from strongly acidic solutions. J. Mater. Chem. A *5*, 13557-13564. https://doi.org/10.1039/C7TA02518A.

6. Muslu, N. & Gülfen, M. (2011). Selective separation and concentration of Pd (II) from Fe (III), Co (II), Ni (II), and Cu (II) ions using thiourea-formaldehyde resin. J. Appl. Polym. Sci. *120*, 3316-3324. https://doi.org/10.1002/app.33509.

7. Zhou, L., Liu, J. & Liu, Z. (2009). Adsorption of platinum (IV) and palladium (II) from aqueous solution by thiourea-modified chitosan microspheres. J. Hazard. Mater. *172*, 439-446. https://doi.org/10.1016/j.jhazmat.2009.07.030.

8. Sharma, S., Barathi, M. & Rajesh, N. (2015). Efficacy of a heterocyclic ligand anchored biopolymer adsorbent for the sequestration of palladium. Chem. Eng. J. *259*, 457-466. https://doi.org/10.1016/j.cej.2014.08.002.

9. Sharma, S. & Rajesh, N. (2014). 2-Mercaptobenzothiazole impregnated cellulose prepared by ultrasonication for the effective adsorption of precious metal palladium. Chem. Eng. J. *241*, 112-121. https://doi.org/10.1016/j.cej.2013.12.002.

10. Kang, T., Park, Y. & Yi, J. (2004). Highly selective adsorption of Pt2+ and Pd2+ using thiol-functionalized mesoporous silica. Ind. Eng. Chem. Res. *43*, 1478-1484. https://doi.org/10.1021/ie030590k.

11. Sayın, M., Can, M. & İmamoğlu, M. (2021). Adsorption of Pd (II) and Au (III) Ions by Commercial Tris (2-Aminoethyl) Amine Polystyrene Polymer Beads. J.Chem. Eng. Data *66*, 1132-1143. https://doi.org/10.1021/acs.jced.0c00920.

12. Sharma, S. & Rajesh, N. (2017). Expeditious preparation of β-cyclodextrin grafted chitosan using microwave radiation for the enhanced palladium adsorption from aqueous waste and an industrial catalyst. J. Environ. Chem. Eng. *5*, 1927-1935. https://doi.org/10.1016/j.jece.2017.03.015.

13. Wang, Z., Kang, S. B. & Won, S. W. (2021). Selective adsorption of palladium (II) from aqueous solution using epichlorohydrin crosslinked polyethylenimine-chitin adsorbent: Batch and column studies. J. Environ. Chem. Eng. *9*, 105058. https://doi.org/10.1016/j.jece.2021.105058.

14. Sayın, M., Can, M., İmamoğlu, M. & Arslan, M. (2015). 1, 3, 5-Triazine-pentaethylenehexamine polymer for the adsorption of palladium (II) from chloride-containing solutions. React. Funct. Polym. *88*, 31-38. https://doi.org/10.1016/j.reactfunctpolym.2015.02.003.

15. Grad, O., Ciopec, M., Negrea, A., Duțeanu, N., Vlase, G., Negrea, P., Dumitrescu, C., Vlase, T. & Vodă, R. (2021). Precious metals recovery from aqueous solutions using a new adsorbent material. Sci. Rep. *11*, 1-14. https://doi.org/10.1038/s41598-021-81680-z.

16. Bai, F., Ye, G., Chen, G., Wei, J., Wang, J. & Chen, J. (2013). Highly selective recovery of palladium by a new silica-based adsorbent functionalized with macrocyclic ligand. Sep. Purif. Technol. *106*, 38-46. https://doi.org/10.1016/j.seppur.2012.12.021.

17. Fujiwara, K., Ramesh, A., Maki, T., Hasegawa, H. & Ueda, K. (2007). Adsorption of platinum (IV), palladium (II) and gold (III) from aqueous solutions onto l-lysine modified crosslinked chitosan resin. J. Hazard. Mater. *146*, 39-50. https://doi.org/10.1016/j.jhazmat.2006.11.049.

18. Sharififard, H., Soleimani, M. & Ashtiani, F. Z. (2012). Evaluation of activated carbon and bio-polymer modified activated carbon performance for palladium and platinum removal. J. Taiwan. Inst. Chem. Eng. *43*, 696-703. http://doi.org/10.1016/j.jtice.2012.04.007.

19. Liu, L., Liu, S., Zhang, Q., Li, C., Bao, C., Liu, X. & Xiao, P. (2013). Adsorption of Au (III), Pd (II), and Pt (IV) from aqueous solution onto

graphene oxide. J. Chem. Eng. Data *58*, 209-216. https://doi.org/10.1021/je300551c.

20. Awual, M. R., Khaleque, M. A., Ratna, Y. & Znad, H. (2015). Simultaneous ultra-trace palladium (II) detection and recovery from wastewater using new class meso-adsorbent. J. Ind. Eng. Chem. *21*, 405-413. https://doi.org/10.1016/j.jiec.2014.02.053.

21. Nagarjuna, R., Sharma, S., Rajesh, N. & Ganesan, R. (2017). Effective adsorption of precious metal palladium over polyethyleneimine-functionalized alumina nanopowder and its reusability as a catalyst for energy and environmental applications. ACS Omega *2*, 4494-4504. https://doi.org/10.1021/acsomega.7b00431.